CHALMERS
UNIVERSITY OF TECHNOLOGY

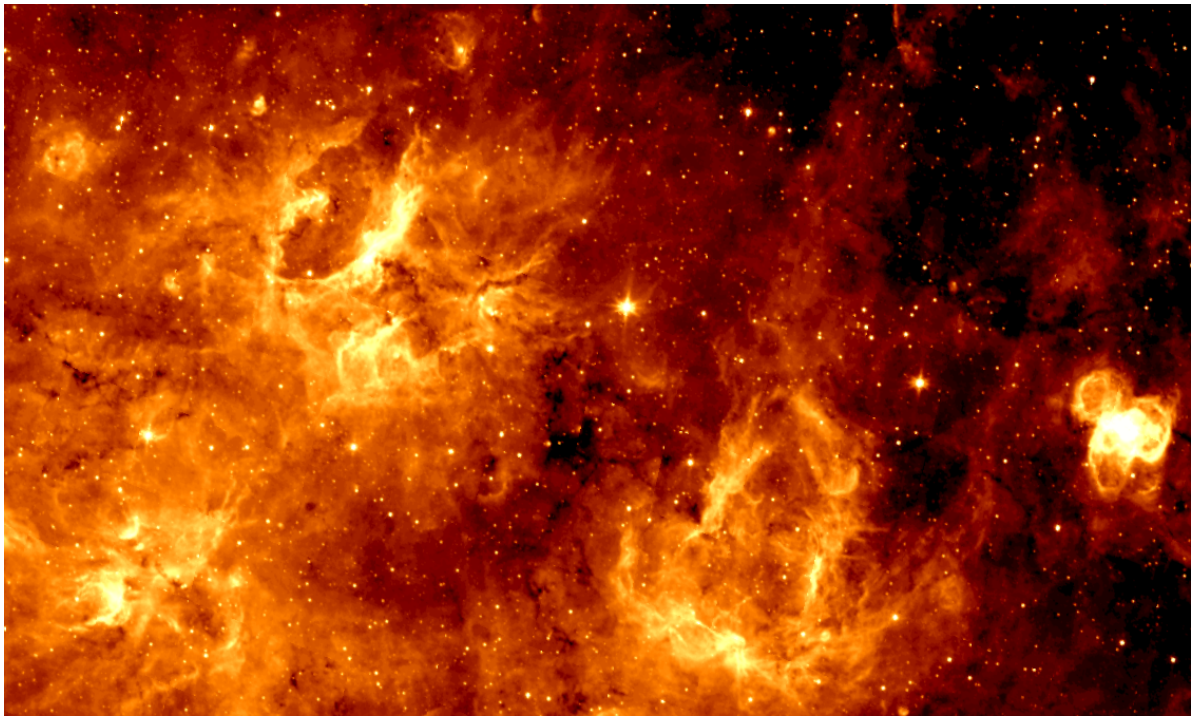

Massive Star Formation in the Infrared Dark Cloud G024.64+00.16

Bachelor thesis in Chemical Engineering with Engineering Physics
SEEX15-21-81

EMMA ULBERSTAD
AXEL LIND
LUDVIG ASKBOM

DEPARTMENT OF SPACE, EARTH AND ENVIRONMENT

CHALMERS UNIVERSITY OF TECHNOLOGY
Gothenburg, Sweden 2021
www.chalmers.se

Massive Star Formation in the Infrared Dark Cloud G024.64+00.16

EMMA ULBERSTAD
AXEL LIND
LUDVIG ASKBOM

Supervisors: Dr. Giuliana Cosentino, Dr. Rubén Fedriani and Dr. Prasanta Gorai,
Department of Space, Earth and Environment
Examiners: Prof. Jonathan C. Tan and Dr. Eva Wirström,
Department of Space, Earth and Environment

Bachelor Thesis 2021
Department of Space, Earth and Environment
Chalmers University of Technology
SE-412 96 Gothenburg
Telephone +46 31 772 1000

Cover: 8 µm image of the IRDC G024.64+00.16 and its surrounding taken by the Spitzer Space Telescope. Image courtesy of JPL/NASA.

Typeset in LaTeX
Printed by Chalmers Reproservice
Gothenburg, Sweden 2021

Abstract

Massive stars drive the energy content and chemical enrichment of galaxies. Despite their importance, it is still not fully understood what mechanisms leads to the formation of massive stars. It is therefore important to study the regions in the universe where massive stars form, infrared dark clouds, to better understand the physical conditions under which massive star formation occurs. In this project we have investigated the kinematic structure, physical conditions and star formation content of the IRDC G024.64+00.16. We have used a mass surface density map obtained from near IR data to investigate the presence of massive cores within the cloud. Multi wavelength images obtained by Spitzer and Hershel have been used to identify the relative evolutionary stage of these massive cores. We have also used ^{13}CO(1-0) and C^{18}O(1-0) maps from the FUGIN survey to investigate the kinematics of the gas at the cloud and core scale. The physical conditions of the cores were determined by calculating the column density, the mass surface density and the depletion for ^{13}CO and C^{18}O. A virial analysis was done to estimate if the gas of the cores are gravitationally bound or unbound. We find that the IRDC contains three cores and that none of these are associated with IR signatures at 4.5, 8, 24 or 70 µm, indicating that these cores are likely at an early relative evolutionary stage. Finally, we find that the cores within the cloud show ^{13}CO and C^{18}O column densities in the range 1.87 - 2.28 $\times$ 10^{16} cm^{-2} and 0.50 - 0.81 $\times$ 10^{16} cm^{-2} respectively, virial parameters α_{vir} >1 and depletion factors in the range 6.15 - 10.13 for ^{13}CO and 2.80 - 6.41 for C^{18}O.

Sammanfattning

Massiva stjärnor ger energi till galaxer och berikar dom med atomer och molekyler. Trots deras viktiga roll är det ännu inte helt förstått vilka mekanismer som leder till att massiva stjärnor bildas. Det är därför viktigt att undersöka de regioner i universum där dessa stjärnor bildas, infraröda mörka moln, för att bättre förstå de fysiska förhållanden under vilka massiva stjärnor bildas. I den här rapporten undersöker vi den kinematiska strukturen samt de fysiska förhållandena i det infraröda mörka molnet G024.64+00.16. Vi har använt en ytdensitetkarta framtagen från kortvågs infraröd data för att undersöka om det finns massiva kärnor i molnet. Bilder framtagna av Spitzer och Hershel i flera våglängder har använts för att avgöra vilket evolutionärt stadie kärnorna befinner sig i. Vi har använt kartor av ^{13}CO(1-0) och C^{18}O(1-0) från FUGIN för att undersöka kinematiken hos molnet och kärnorna. De fysiska tillstånden hos kärnorna avgjordes genom att beräkna kolumndensiteten, massdensiteten och utfrysningsfaktorn för ^{13}CO och C^{18}O. En virialanlys gjordes för att avgöra om kärnorna är bundna av sin gravitation eller inte. Vi fann att molnet innehåller tre kärnor och att ingen av dessa är associerade med de infraröd signaturerna av 4.5, 8, 24 or 70 µm, vilket tyder på att dessa kärnor befinner sig i ett tidigt evolutionär stadie. Till sist finner vi att kärnorna i molnet visar en ^{13}CO och C^{18}O kolumndensitet inom spannet av 1.87 - 2.28 $\times$ 10^{16} cm^{-2} and 0.50 - 0.81 $\times$ 10^{16} cm^{-2} respektive, virial parametrar α_{vir} >1 samt utfrysningfaktorer inom spannet av 6.15 - 10.13 för ^{13}CO and 2.80 - 6.41 för C^{18}O.

Contents

1 Introduction

Mankind has always been fascinated by stars, and for millennia the night sky has amazed us and filled us with wonder. Stars have an immense cultural, religious and scientific value, and understanding how they come to be seems only natural to our curious nature. Everything around us, and everything we are made up of is due in part to stars. Most atoms in the universe were forged through nuclear fusion in the cores of stars (Shore 2003), or in their dramatic final breaths, like supernova explosions. These giants roam the universe supplying galaxies with energy through stellar winds, UV-radiation and jets. They may also continue to affect their surroundings long after their death. Even black holes, that make up the center of galaxies, are theorized to stem from the remnants of a massive star.

1.1 Massive Stars and their Observational Challenges

Stars can be divided into three groups: Low-mass, intermediate-mass and massive stars. Low-mass- and intermediate-mass stars are numerous in the universe, and much like our own Sun, are relatively small in cosmic terms (Rosen et al. 2020). Massive stars are much bigger with a mass $8 > M_{\odot}$, meaning eight times that of our own Sun, on top of being much rarer (Frost et al. 2021). Low-mass stars are well studied and we have a good understanding of how they form (Luhman 2011). Much about the early stages of massive star formation is however still unknown.

Studying the early stages of massive stars comes with a number of problems. Massive stars are more difficult to observe since they evolve quickly and their critical evolutionary phases are short lived compared to their low-mass counterparts (Zinnecker & Yorke 2007). For a low-mass star to enter its main sequence, the point where hydrogen fusion begins, it will usually require $10^7 - 10^8$ years. A massive stars on the other hand only requires $\sim 10^5$ years (Yamamoto 2017). This means that massive stars are enshrouded in gas and dust for a larger part of their accretion process (Frost et al. 2021). The fact that massive stars are much rarer than low-mass stars also implies that the nearest objects lie further away which further complicates observations (Evans II 1999, Rathborne et al. 2010). Most massive stars are believed to form in clusters, and this combined with the increased distance makes separation of events in these regions more difficult. Massive stars also have a bigger influence on their surrounding making it more difficult to determine the prerequisites for their formation.

It is thought that all stars arise as a result of the denser regions of giant molecular clouds (GMCs) collapsing under their own gravity (Carroll & Ostlie 2014). For a GMC to collapse it needs to reach a critical density. There are several theories regarding how this might happen, such as density fluctuations as a result of clouds colliding with each other (Tasker & Tan 2009), the cloud being stricken by a shock wave from a nearby supernova (Inutsuka et al. 2015) or simply the turbulence and rotation of the cloud itself (Chevance et al. 2020). Once the cloud has collapsed the evolution starts to differ between low-mass stars and massive stars. Both types of cores will continue to accrete mass from their surrounding envelope of gas and dust.

A low-mass core will during this stage go through a second collapse as the core is heated and will come out as a protostar which continues to accrete mass from its surrounding (Yamamoto 2017). The mass will typically fall in to the core via an accretion disc, a spinning disc of matter surrounding the core. As the matter falls in to the core it carries with it angular momentum which the core needs to transport. This could be done through jets, outflows perpendicular to the accretion disc which expel matter from the core (Frank et al. 2014). Eventually the protostar depletes its surrounding envelope of gas and dust and begin to fuse hydrogen and enters its main sequence.

It is not certain that massive stars follow the same early evolutionary stages as low-mass stars (Evans II 1999, Yamamoto 2017). Due to their larger mass, the outward pressure imparted by photons released by the accreting matter is much larger for massive protostars than that of low-mass protostars. This increased outward force should hinder cores from accreting enough mass to become massive. Massive protostars also display outflows which release matter at such a rate that it is uncertain how enough mass is accumulated for stars to become massive.

There are two main theories regarding how this accretion could occur. *Core accretion* is an extension of low-mass accretion theory (Tan et al. 2014). According to this theory, a cluster of cores form at the center of the collapsing region due to fragmentation. These cores then collapse in to the center via a central disc and result in a massive core. *Competitive accretion* claims that the needed matter is drawn from a wider region (Yamamoto 2017). This means that *competitive accretion* is a much more chaotic process than *core accretion* as the gas being accreted is not gathered in a massive coherent center. The theory continues that massive cores first form as a member of a cluster of low-mass cores. Cores located at the center of the collapsing cloud have a lower gravitational potential and can therefore gather more mass from their parent cloud and surrounding low-mass stars.

In either case, the core will at some point become so hot and dense that it ignites, and the star enters its main sequence. Throughout the life of a massive star an immense amount of energy is released through nuclear fusion. This energy is what keeps the star from collapsing under its own gravity. Once the star begins to fuse iron the energy released from fusion is no longer sufficient to withstand the forces of gravity and the star collapses (Fraknoi et al. 2016).

Currently, the best way we have of studying the earliest evolutionary stages of massive stars is to study the environments in which they are believed to form. The formation of massive stars are believed to require a very cold and dense environment, and the densest regions of GMCs are called infrared dark clouds (IRDCs) (Rathborne et al. 2010, Chira et al. 2013). Through this project we wish to further our understanding of the conditions necessary for massive stars to form and the process as such. By studying an IRDC that may harbor massive stars in their earliest stages, we wish to gain more insight into how massive stars come to be.

1.2 IRDCs: Composition, Formation and Compression

IRDCs consist of gas and dust packed so dense that they appear as dark silhouettes against the bright mid-infrared background (Rathborne et al. 2010). IRDCs consist mainly of H, H_2 and CO (Yamamoto 2017). Besides these, there are a great variety of molecules present in IRDCs such as CN and CS. Different molecules can act as tracers for different properties of

the IRDC. For instance, SiO is a good tracer for shocked gas (Miettinen 2012), CO is good tracer for mass (Evans II 1999) and CH_3CN is a very good tracer of warm and dense regions (Vasyunina et al. 2011). Studies have shown IRDCs to be very cold with temperature below 25K (Vasyunina et al. 2009), and dense with a density greater than 10^4 molecules cm^{-3} (Egan et al. 1998). These conditions can result in the CO gas freezing onto the dust particles in the IRDC, thus becoming solid. This process is called CO depletion (Hernandez et al. 2011) and is measured with a depletion factor f_D, i.e. the ratio between the expected and the measured CO abundances. For star forming IRDCs, the depletion factor is usually in the range of 1-10 (Sabatini et al. 2019).

There are three main theories regarding how IRDCs can form and collapse. The first is called the theory of *gravitational collapse* (Chevance et al. 2020). It says regions of higher density will inevitably form within the GMC. The increased density of these regions then creates a stronger gravitational force on its surroundings causing it to continue to gain mass and contract. The region will at some point be dense enough to be considered an IRDC. This gravitational contraction can then, depending on the mass available, continue until the IRDC collapses into a core.

Another theory is the *cloud-cloud collision* theory (Tasker & Tan 2009). It states that when traveling within a galaxy, clouds can sometimes collide causing the gas in the clouds to be compressed and form denser regions. These regions can then, depending on what density they reach, continue to form an IRDC in a similar manner as the previous theory.

The third theory is that *shock waves from supernovae* can cause the cloud to grow denser (Inutsuka et al. 2015). The theory states that the matter and energy expelled by a supernova traveling through space can impact a cloud and that this can cause the cloud to become denser. These denser regions might then similarly form an IRDC and collapse into cores. It is important to note that these theories are not exclusive to each other and they may all be correct for certain cases and sequence of events.

1.3 IRDC Collapse

In order to collapse, a clouds needs to be compressed to the point where internal gas pressure cannot compete with the clouds gravitational potential (Carroll & Ostlie 2014). This is stated by the virial theorem, defined as

$$2K + U = 0 \tag{1.1}$$

where K is the kinetic energy of a molecular cloud and U is the gravitational potential energy. The theorem tells us that if two times the kinetic energy of the cloud exceeds the absolute value of the gravitational potential energy the molecular cloud will expand. If the gravitational potential energy exceeds two times the kinetic energy, gravity will overcome the gas pressure and the cloud will collapse under its own gravity. The virial theorem allows us to define the Jeans length. The Jeans length is the minimum size of a cloud capable of collapse. If the radius of the cloud is smaller than the Jeans length it will not collapse due to the gas pressure being bigger than the gravitational force, causing the cloud to expand (Ridpath 2012). When the radius is equal to the Jeans length the cloud neither expands nor compresses. Each

Jeans length has a corresponding Jeans mass, the mass contained within the Jeans length and therefore the minimum mass required for the cloud to be able to collapse. From this we can derive the time it takes for the cloud to collapse if it collapses in free-fall denoted as t_{ff} (Carroll & Ostlie 2014). It should be noted that this time is only valid if we assume that the cloud is acting solely under the influence of its own gravity and in the absence of internal pressure. If the occurrence of clouds collapsing under free-fall conditions was common, the total mass of stars formed per year, i.e star formation rate, would be greater than 200 $\text{M}_{\odot}\text{yr}^{-1}$ (Evans II 1999). The observed average star formation rate is about 3 $\text{M}_{\odot}\text{yr}^{-1}$, meaning that a vast majority of collapses do not occur under free-fall conditions. They are slowed by the cloud's internal pressure, especially in its early stage (Larson 1969). Surveys have also shown that turbulence and the cloud's magnetic field can play a part in slowing down the collapse (Evans II 1999). Regardless of its flaws, free-fall time gives us a good estimation of the time for a collapse. In a GMC with a mass of about $10^5 - 10^6 M_{\odot}$ the free-fall time varies from $t_{\text{ff}} \sim 3$ Myr to $t_{\text{ff}} \sim 0.1$ Myr for values of gas number density n varying from $n \sim 10^2\text{cm}^{-3}$ to $n \sim 10^5\text{cm}^{-3}$ (Chevance et al. 2020). As the cloud collapses the density of the cloud increases and the Jeans length and mass decrease. This results in smaller regions within the original collapsing region to also collapse. This is called fragmentation and allows for several cores to form in the same region.

1.4 Molecular and Infrared Tracers

Once cores have formed they will first appear as infrared sources surrounded by gas and dust (Carroll & Ostlie 2014). The wavelength of the infrared light emitted depends on which stage in its evolution the core is currently in. By analysing the areas inhabited by suspected cores in different wavelengths we can draw conclusions about what relative evolutionary stage each core is currently in. In this project we will examine possible cores in four different wavelengths: 4.5 µm, 8 µm, 24 µm and 70 µm. If a core shows emissions at 4.5 µm it suggests that the core is emitting jets of material (Noriega-Crespo et al. 2014). If the core emits a wavelength of 8 µm it may be because of emissions from excited polycyclic aromatic hydrocarbons (PAHs) (Tielens 2013). PAHs are only exited in regions with intense ultraviolet radiation, therefore 8 µm radiations indicates that the core is in a later relative evolutionary stage where massive stars have already formed and started to emit ultraviolet radiation. Emissions at 24 and 70 µm are signifiers of thermal radiation emitted by dust particles of varying size in the infalling envelope surrounding the core. The emissions are caused by gravitational energy being converted into thermal energy, in turn heating up the dust (Gutermuth & Heyer 2015). The smaller dust particles re-emit at 24 µm, and bigger particles at 70 µm. If no emission is shown in these wavelengths, there is a chance the core is starless (Pillai et al. 2019). Starless regions are thought to contain precursors of massive stars.

Observing light emitted from a single molecule can also be a good way of acquiring information about the IRDC. GMCs consist mainly of H_2. Absorption of H_2 requires ultraviolet radiation from background stars, this is however only possible for the H_2 on the surface of the cloud as the dust in the cloud stops the ultraviolet light from penetrating to the bulk of the cloud (Evans II 1999). This means that we can only use this molecule to map the surface of the cloud.

This is why almost all surveys of GMCs have other molecules besides H_2. The second most abundant molecule in GMCs is carbon monoxide, CO (Evans II 1999), and this is consequently the most commonly used tracer of molecular gas. In dense regions such as IRDCs however, normal CO becomes optically thick according to Kennicutt & Evans (2012), meaning that the light cannot penetrate the IRDCs. As they put it, using CO as a tracer is "[...] akin to using the presence of a brick wall to estimate the depth of the building behind it". Instead, isotopologues of CO are used. The two isotopologues used in this report are ^{13}CO and C^{18}O. ^{13}CO is the more abundant of the two (Wilson & Rood 1994) and is therefore commonly used as a tracer for the IRDCs structure and its kinematics. While ^{13}CO runs the risk of becoming optically thick towards the densest regions, it can be mapped further out in thinner regions making it a better tracer for overall structure (Ridge et al. 2003). This is why Section 3 focuses mainly on data extracted from ^{13}CO. As one of the less abundant isotopologues, C^{18}O gives a more accurate estimate of the depletion f_D (Sabatini et al. 2019) since it avoids the problem of optical thickness (Goldsmith et al. 1997).

The kinematics of the gas in a cloud and the surroundings of cores can tell us about their formation and early evolution (Wu et al. 2017). The Doppler effect, the physical phenomenon when a waves frequency changes depending on the movement of its source, allows for the extraction of velocity spectra for the cloud and its different parts (Carroll & Ostlie 2014).

1.5 The IRDC G024.64+00.16

In this report we will specifically study the IRDC G024.64+00.16. No previous studies have been done on this IRDC, therefore there are no results to compare with our own. The IRDC is moving towards us at a mean velocity of 51.3 $\mathrm{km\,s^{-1}}$ and lies at a distance of 3.36 kpc from us (Cosentino, private communication).

1.6 Aim and Thesis Outline

The aim of this project is to investigate the level of star formation activity, kinetic structure and physical conditions of the IRDC G024.64+00.16. This includes studying whether the cloud contains cores and if so, determine if these cores are protostars, stars in the main sequence or if the core is quiescent by analysing the emitted wavelengths of the IRDC. We will study how the IRDC moves through analysing its kinematic. Lastly, we will calculate the physical conditions of the IRDCs and cores to find out things such as mass, depletion of CO and the gravitational stability. The information obtained will help to constrain the physical conditions required to form massive stars in IRDCs.

The project will be limited to the study of one IRDC and only the question of regarding massive star formation will be evaluated. Questions such as how the IRDC is formed or what happens to the cores after their formation will not be studied in detail. The limitation of studying a single IRDC means that the result will only provide limited knowledge. No conclusions on how all massive stars are formed in IRDCs can be obtained as the circumstances may differ in other IRDCs. Gathering information about more IRDCs can however lead to a better understanding of massive star formation as a whole. The beam size and therefore the

angular resolution of the images of the IRDC also induces some limitations with regards to the precision of the results.

Furthermore, a kinematic analysis will only be done for CO data. This limitation could skew the result somewhat, but since CO is the second most abundant molecule in the IRDC the result should still be sufficiently accurate. Only two isotopologues of CO will be studied, ^{13}CO and C^{18}O. This will limit us as these isotopologues do not trace all properties of the IRDC.

This thesis we will divided into three chapters pertaining to the methods that will be performed. These chapters are divided based on the results that they aim to produce. In Chapter 2 we focus on Massive Core Identification, in Chapter 3 we investigate the Kinematics structure of the IRDC, and in Chapter 4 we focus on the Physical Conditions of the molecular gas in the IRDC. In each chapter a short introduction will be given stating the general aim. This will be followed by detailed description of the methods used to obtain the results. The results will then be presented with relevant figures and tables, after which a short conclusion will be made. This format will follow through for all three chapters. Finally, in Chapter 5 a discussion of the results will be presented and in Chapter 6 we summarize our conclusions.

2 Massive Core Identification in the IRDC G024.64+00.16

This section focuses on investigating the presence of massive cores within the IRDC 024.64+00.16 and their relative evolutionary stage. This will be done by using multi-wavelegth images and a mass surface density map. This Chapter is organized as follows: in Section 2.2 the mass surface density map is introduced. In Section 2.3 the massive cores are identified, and in Section 2.4 the relative states of these cores is determined.

2.1 Dataset

Images of the IRDC 024.64+00.16 used in Section 2.4 were obtained from the Spitzer Space Telescope and Herschel Space Observatory. Images from Spitzer were taken in 4.5 µm, 8 µm and 24 µm utilizing the IRAC2, IRAC4 and MIPS1 channel respectively. Spitzer has an angular resolution of 20″ and a pixel size of 0.6″. The 70 µm Herschel image was taken with the PACS instrument and has a pixel size of 3.2″. These images were accessed with the interactive sky atlas Aladin (Bonnarel et al. 1998). Aladin functions as an interactive application for astronomical images and data from the SIMBAD database. The mass surface density map used in Section 2.2 and 2.3 was derived from 8 µm images taken by Spitzer. The mass surface density map has an angular resolution of 20″ and a pixel size of 0.6″.

2.2 Mass Surface Density Map

A map of the mass surface density, Σ, of the IRDC was used. The map had been produced from 8 µm images taken by the Spitzer Space Telescope and applying the method described by Butler & Tan (2009). As reported by the authors, 8 micron images were used to model the background infrared (IR) emission toward the cloud and hence infer the level of visual obstruction (visual extinction) caused by the dense material of the source. The extinction map was then converted into a mass surface density map (see Kainulainen & Tan 2013). The visualization tool for astronomical data, SAOImageDS9, was used to display the mass surface density map (Joye & Mandel 2003). The mass surface density map of the IRDC is shown in Figure 2.1. The central coordinates of the map are RA: 18:35:39.3077, Dec: -7:17:46.893 (J2000).

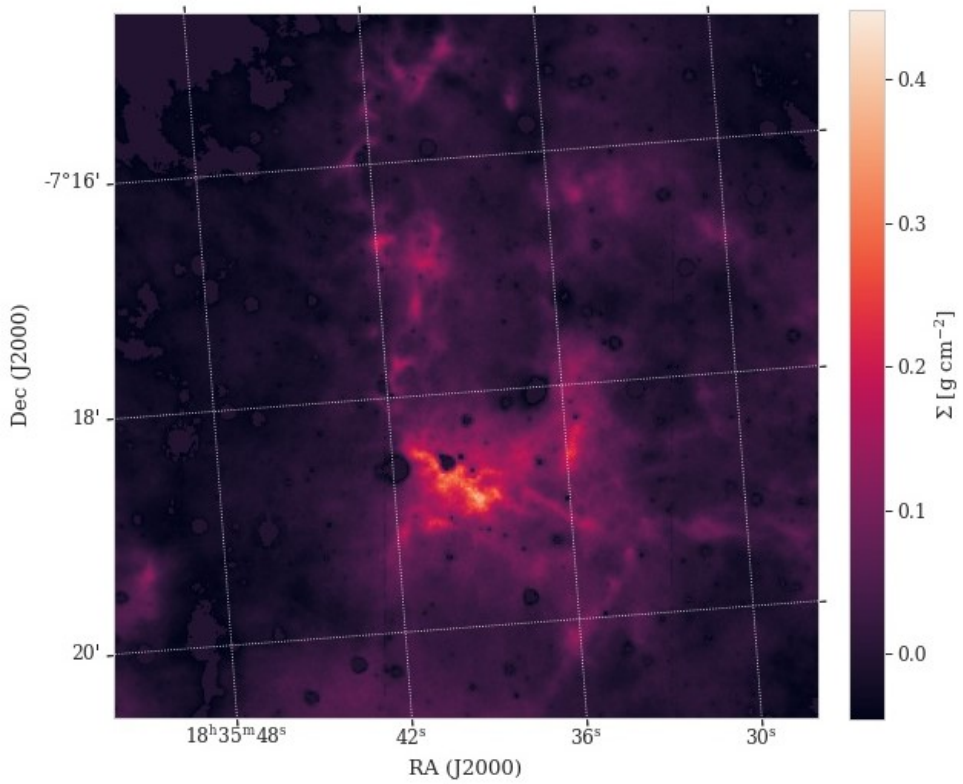

Figure 2.1: Mass surface density map of the IRDC G024.64+00.16. The map has an angular resolution of 20″ and a pixel size of 0.6″.

As shown in Figure 2.1, regions as dense as 0.3-0.4 g cm^{-2} can be identified. In addition, dark spots are seen toward several location across the map. These are bright 8 µm source (probably stars), not associated with the IRDC, whose emission have been removed from the map since the method adopted by Butler & Tan (2009) cannot be applied to very bright features.

2.3 Massive Core Identification

In order to identify massive, dense cores within the IRDC, we performed a dendrogram analysis of the mass surface density map. Dendrogram analyses are used to identify structures within a 2D or 3D dataset and the hierarchical relation between them by implementing the method used in Rosolowsky et al. (2008). A dendrogram divides the mass surface density map into branches and leaves with regards to pixel brightness and constructs a tree structure where regions of local brightness maximum can easily be observed. The dendrogram can also give us information that help us determine if a local maximum observed is due to a massive core or due to some disturbance by observing its shape and relative position in the IRDC. Figure 2.2 shows a simple example of how a dendrogram (right) is constructed from a density map (left).

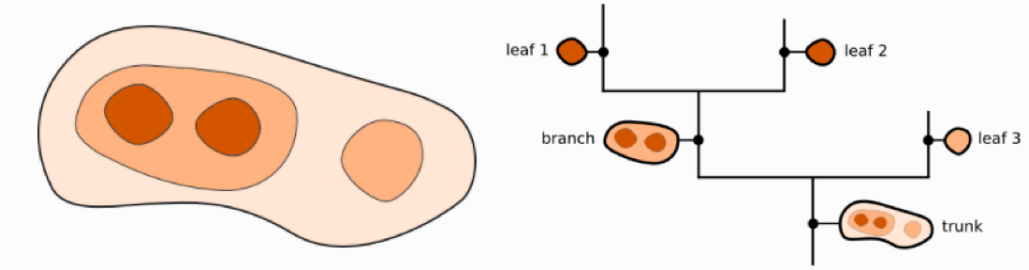

Figure 2.2: Simple example of a density map (left) and its corresponding dendrogram (right). The figure illustrates the difference between trunks, branches and leaves. Image courtesy of the *Astrodendro Documentation*

In the map shown in Figure 2.2 a darker color represents a higher pixel brightness. The dendrogram identifies the different levels of pixel brightness and divides these in to trunks, branches and leaves. This division can be seen on the right in the figure with leaves being the smallest and brightest hierarchical structure.

The *astrodendro* Python library is an implementation of the method laid out in Rosolowsky et al. (2008) and was used to construct the dendrogram. The algorithm requires the user to define a set of parameters to perform the analysis. `min_value` sets a lower limit for where the tree structure begins. `min_delta` sets the lowest difference in pixel brightness that a branch or leaf can have to be considered a separate entity. `min_npix` sets the lowest number of pixels that can make up a leaf. The `min_npix` value can then be calculated as

$$\texttt{min\_npix} = \frac{A_{beam}}{A_{pixel}} \tag{2.1}$$

Using the properties from Section 2.1 we obtain `min_npix` = 9 px.

For the remaining two values we follow the method presented in Cheng et al. (2018) where the authors use `min_delta` = 1σ and `min_value` = 4σ, with σ being the map noise. To determine the noise, a region outside the IRDC was selected and the mean intensity of this region was measured. This results in a statistical noise of 0.0384 gcm^{-2}. Due to assumptions in the method applied when converting the 8 µm image to a mass surface density map, systematic errors must be accounted for. Our method has systematic errors of about 20-25%. This results in a noise value of 0.05-0.06 gcm^{-2}. The value of 0.06 gcm^{-2} was chosen as the final noise value. We then obtain `min_value` = 0.24 g cm^{-2}. With these values the final dendrogram was constructed, and is shown in Figure 2.3 together with the mass surface density map. Due to the systematic errors being uncertain, we estimated how noise fluctuation affected the results of the dendrogram. The resulting dendrograms were compared to the initial one. This was done to determine whether a leaf observed in the dendrogram was representative of a core, or if it should be disregarded. If a leaf separates or merges with another when varying the noise, it is an indication that the leaf may not represent a core since they are not stable within the predetermined range of error. Varying the level of noise resulted in core 4 splitting into two separate cores. The splitting of core 4 was not considered problematic due to its location next to an object between us and the IRDC, this is discussed further in Section 5.1.

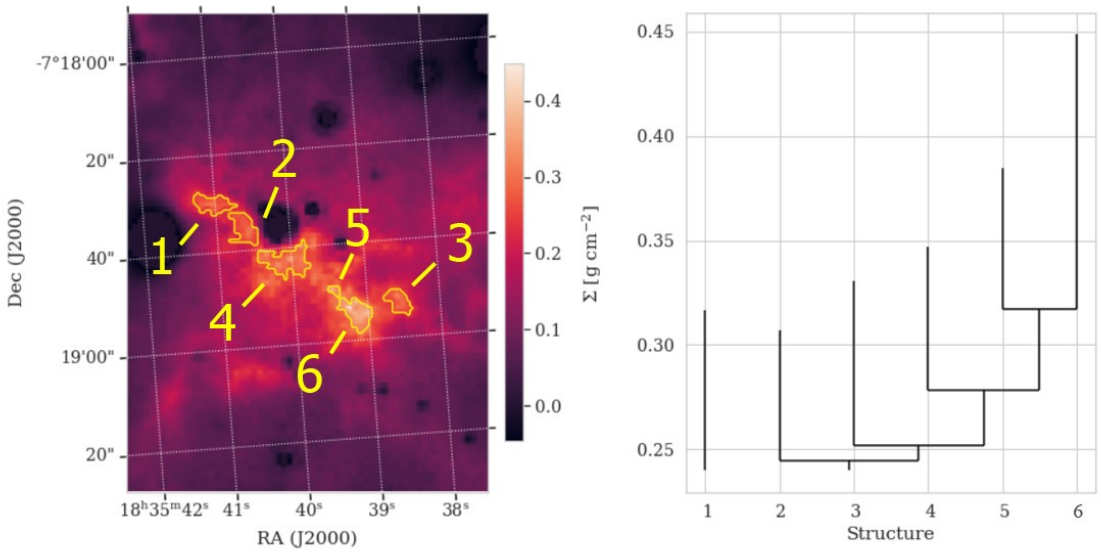

Figure 2.3: Mass surface density map (left) of the IRDC and the constructed dendrogram (right). The leaves of the dendrogram, labeled as structures, are shown in the density map as yellow contours.

As seen in Figure 2.3, six leaves are identified. Structure 5 is relatively small in comparison to the other structures, and it appears to be connected with structure 6. The cores identified as 2 and 4 in Figure 2.3, appear close to a dark spot in the mass surface density map. This dark feature corresponds to a bright IR source in the 8 µm map and is characterized by a negative intensity on the map. The dendrogram analysis may be affected by this and cores 2 and 4 may only be tracing part of the dense gas around this bright source. The validity of the individual structures is further discussed in Section 5.1. The central coordinates and mass of the six identified leaves are presented in Table 2.1. The mass was obtained from multiplying the mass surface density with the area of the beam.

Table 2.1: The central coordinates and of the identified cores in Figure 2.3 are presented in equatorial coordinates together with the mass of each core.

	RA (J2000)	Dec (J2000)	M ($M_\odot$)
Core 1	+18:35:41.0746	-7:18:29.312	63.7
Core 2	+18:35:40.5780	-7:18:35.514	67.2
Core 3	+18:35:38.5879	-7:18:51.662	81.3
Core 4	+18:35:40.1164	-7:18:43.289	85.3
Core 5	+18:35:39.4696	-7:18:49.257	97.6
Core 6	+18:35:39.1658	-7:18:53.429	98.0

As seen in Table 2.1, all cores show masses of 60-100 $M_\odot$. This is consistent with what measured in other sources (e.g. Moser et al. 2020, Nguyên Luong et al. 2011).

2.4 Analyzing the State of the Cores

To analyze the state of the cores, images of the IRDC taken in 4.5, 8, 24 and 70 µm were used. The significance of these wavelengths is explained in Section 1.4. The images were then compared to the mass surface density map. In particular, the position of the identified leaves was compared with those of point-like sources in the multi-wavelengths images.

Figure 2.4 shows images taken in 4.5, 8, 24 and 70 µm obtained from Aladin. The figure also shows the cores obtained from Figure 2.3 overlaid as yellow contours.

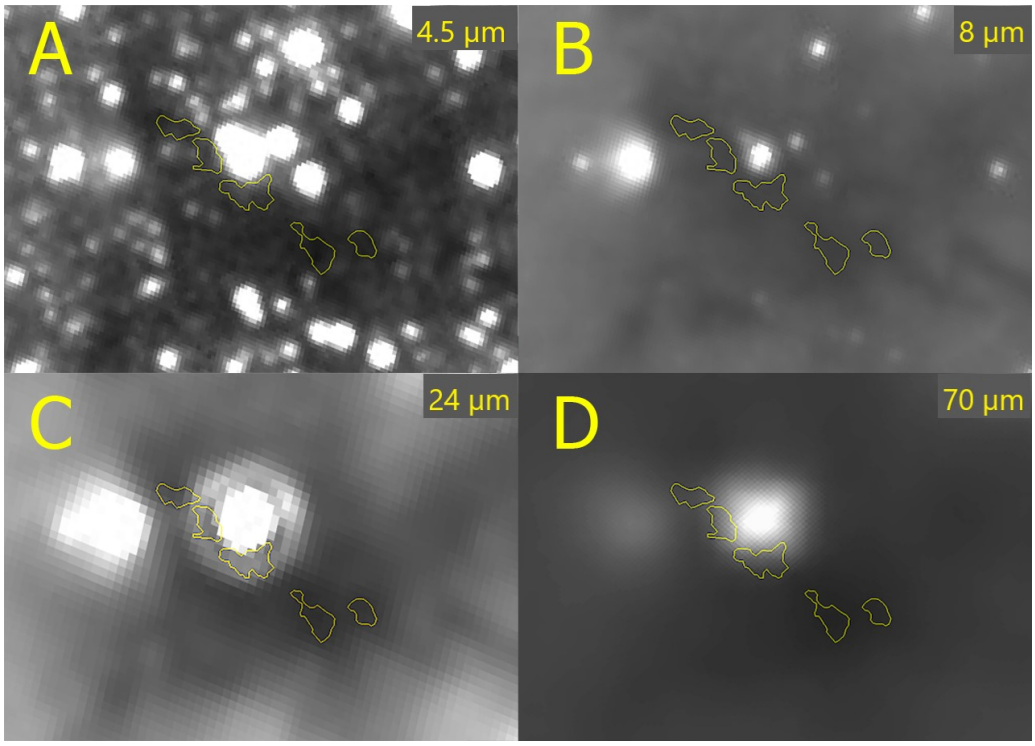

Figure 2.4: The outline of the cores obtained from Figure 2.3 are shown overlaid on images taken in four wavelengths. Images A)-C) were taken with the Spitzer Space Telescope, and D) with the Herschel Space Observatory. Image A) was taken in 4.5 µm with the IRAC2 channel. Image B) was taken in 8 µm with the IRAC4 channel. Image C) was taken in 24 µm with the MIPS1 instrument. Image D) was taken in 70 µm with the PACS instrument. The images taken with Spizer has a pixel resolution of 0.6″, and Herschel 3.2″.

As shown in Figure 2.4, the cores 1, 2 and 4 are likely associated with a bright star showing IR emission at all wavelength. Hence, it is likely that these leaves are not real cores but mostly substructures of a single star forming point-like source. On the other hand, cores 3, 5 and 6 appear relatively isolated with no bright sources in their immediate surrounding. A more detailed discussion is provided in Section 5.1.

Table 2.2 shows what wavelengths are emitted by each core, where Y indicates yes and N indicates no.

Table 2.2: Table of whether the cores identified in Figure 2.3 show emissions of the different wavelengths (Y/N).

	4.5 µm	8 µm	24 µm	70 µm
Core 1	N	N	Y	N
Core 2	N	N	Y	Y
Core 3	N	N	N	N
Core 4	N	N	Y	Y
Core 5	N	N	N	N
Core 6	N	N	N	N

As is shown in Table 2.2, cores 1, 2 and 4 show some emissions within their contours. These emissions are however believed to be from another object between us and the IRDC, this is discussed in Section 5.1.

2.5 Conclusion from Massive Core Identification

We identified six cores using a mass surface density map and dendrogram. Out of these six, cores 1, 2 and 4 were considered to all be tracing dense material surrounding a bright IR source seen at all wavelengths, this is further discussed in Section 5.1. Cores 3, 5 and 6 did not show emissions at any of the surveyed wavelengths: 4.5, 8, 24 and 70 µm. Hence, cores 3, 5 and 6 may be at an earlier evolutionary stage with either no central source or with this still being deeply embedded, so that IR signatures are not detected.

3 Kinematic Structure of the IRDC G024.64+00.16

The kinematic structure of the gas in and around IRDCs can offer good insight into how its moving and behaving. This section investigates the kinematics of the ^{13}CO and C^{18}O toward the potential cores, the IRDC and surrounding GMC. For all those regions, spectra of the two molecular species show multiple velocity components that have been identified by means of multi-Gaussian fittings. Hence, the spatial association between the molecular cloud and the ^{13}CO/C^{18}O gas has been studied by means of integrated intensity maps.

3.1 Dataset

Maps of the ^{13}CO(1-0) and C^{18}O(1-0) emission were obtained as part of the large survey FUGIN (Umemoto et al. 2017) using the Nobeyama 45-m Telescope. Observational parameters include an angular resolution of $20''$ and a pixel size of $8.1''$.

3.2 Kinematic Analysis of the IRDC

In this section we will analyze the kinematic properties of the IRDC. In Section 3.2.1 This will be done by first extracting the ^{13}CO and C^{18}O 1-0 rotational spectra towards the IRDC. We will in Section 3.2.2 fit multi-Gaussian functions to the spectral peaks. Integrated intensity maps of the IRDC and the wider GMC will then be constructed in Section 3.2.3.

3.2.1 Extracting the CO Data

To investigate the kinematics of the IRDC and surrounding GMC, we analyzed the spectral lines of the 1-0 rotational transition of ^{13}CO and C^{18}O. The rest frequency of these transitions are $\nu = 110201\,\mathrm{M\,Hz}$ for ^{13}CO, and $\nu = 109782\,\mathrm{M\,Hz}$ for C^{18}O. The CO data are spectro-imaging cubes, which means that we can extract a spectrum at a give location and/or produce an image at a given frequency or velocity.

The mean velocity of the IRDC is 51.3 $\mathrm{km\,s^{-1}}$, thus the most interesting regions of the spectra are peaks in close vicinity of this velocity. The extracted ^{13}CO and C^{18}O spectra for the IRDC are shown in Figure 3.1.

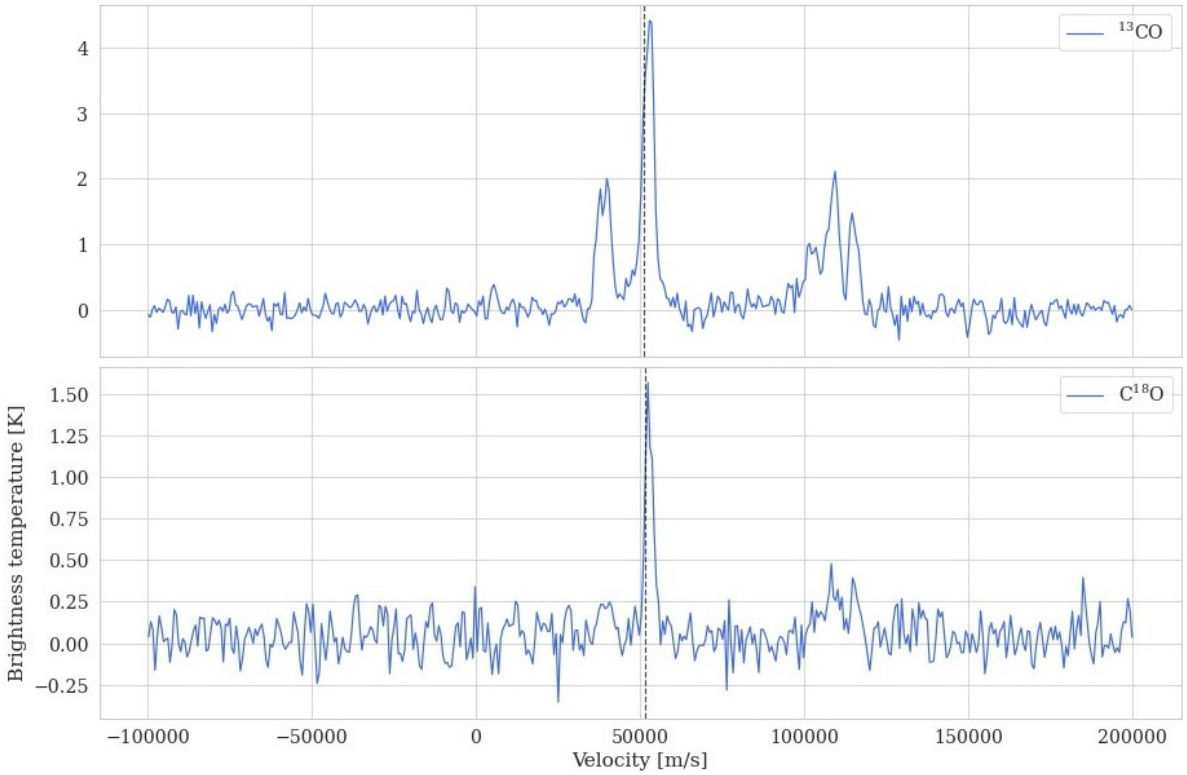

Figure 3.1: The extracted ^{13}CO (top) and C^{18}O (bottom) spectrum for the IRDC G024.64+00.16 shown for the entire velocity range. The cloud's average velocity is marked as a gray dashed line at 51.3 km s^{-1}.

The extracted ^{13}CO spectrum shows one significant peak at ∼53 km s^{-1}. Besides this one, two groups of peaks are located at ∼ 40 km s^{-1} and ∼ 110 km s^{-1}. Since the cloud is moving at 51.3 km s^{-1}, the velocity peak around 53 km s^{-1} is the one corresponding to the ^{13}CO associated with the IRDC. This is also supported by Figure 3.7 and 3.6 in Section 3.2.3. C^{18}O shows only one major peak at around 53 km s^{-1}. Also noticeable is that this spectrum has a smaller peak intensity than the ^{13}CO spectrum.

In order to assure that the spectral peaks observed in the CO data were statistically significant, and not just due to noise, the following test was performed. The test consists of comparing the area of the noise, denoted by A_{RMS} with the area of the observed spectral peak, denoted by A_{Gauss}. A_{RMS} is calculated as

$$A_{\mathrm{RMS}} = 3 \times \mathrm{RMS} \times \sqrt{\mathrm{FWHM} \times dv} \tag{3.1}$$

where RMS is the root mean square of a region of the spectrum containing only noise, FWHM is the Full width at half maximum of the spectral peak and dv is the velocity resolution of the CO data in km s^{-1}. The factor 3 is a statistical factor pertaining to the test in order to be accurate for three times the standard deviation from the mean. The values are then compared according to $A_{\mathrm{RMS}} < A_{\mathrm{Gauss}}$. If the statement holds true, the spectral peak is considered statistically differentiable from the noise. The peak at 53 km s^{-1} in both spectra satisfied this

criteria. The two groups of peaks located at 40 km s^{-1} and 110 km s^{-1} in the C^{13}O spectrum also satisfied the criteria.

3.2.2 Gaussian Fitting to Spectra

In order to understand the velocity distribution of the extracted CO spectra, we investigated their components by means of fitting single- and multi-Gaussian functions. The number of Gaussian functions required was qualitatively assessed based on the shape of the peak. In Figure 3.2 a multi-Gaussian fit to the extracted ^{13}CO spectrum with four components is shown. A multi-Gaussian fit to the extracted C^{18}O spectrum with two components is also shown in Figure 3.2. The spectrum has been zoomed in on a velocity range of 30-64 km s^{-1}.

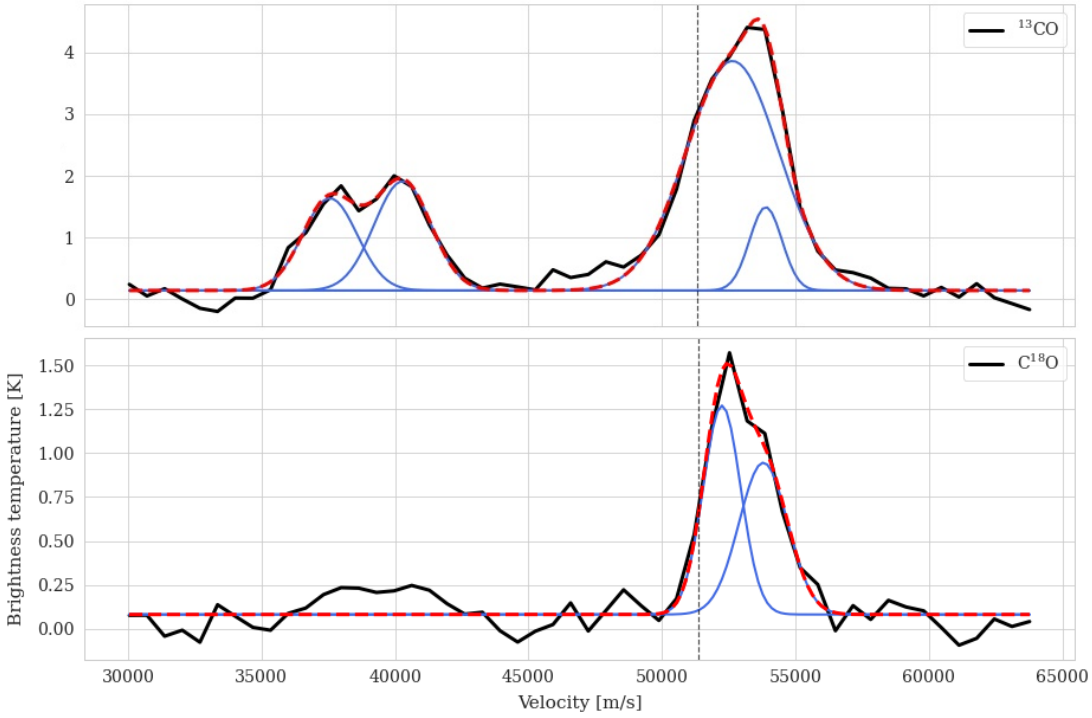

Figure 3.2: Gaussian fits for the extracted spectra towards the IRDC G024.64+00.16. The ^{13}CO line (top) has been fitted with a multi-Gaussian function with four components, and the C^{18}O (bottom) with a multi-Gaussian function with two components. The spectra are shown for a range spanning 30-64 km s^{-1}. The black lines are the unaltered data, the red dash lines is the sum of the individual blue Gaussian functions. The ^{13}CO multi-Gaussian showed a $\chi^2_{red} = 0.151$, and the C^{18}O showed a $\chi^2_{red} = 0.010$. The cloud's velocity is marked as a gray dashed line at 51.3 km s^{-1}.

The Gaussian fit for the ^{13}CO peak at 53 km s^{-1} shows a large Gaussian making up the majority of the shape, combined with a smaller Gaussian to the side. The fit for the peaks at $\sim$38 km s^{-1} was done to illustrate that these are not connected to the peak at 53 km s^{-1}. The C^{18}O fit shows two similarly sized Gaussians making up the peak at 53 km s^{-1}. The overall shape of this peak seems to be inverted compared to the equivalent ^{13}CO peak, but this could be due to issues with the velocity resolution.

The Gaussian fit to the data was also tested by calculating a χ^2_{red} value. The χ^2 test is used as a metric for how much a fit deviates from the observed data. When comparing data sets of different frequency the reduced version is commonly used, whereby you divide by the degrees of freedom. A χ^2_{red} metric was calculated for all Gaussian fits according to the definition

$$\chi^2_{red} = \frac{\chi^2}{n-p} = \frac{\sum_{i=1}^{n} \frac{(y_i^{obs} - y_i^{exp})^2}{y_i^{exp}}}{n-p} \tag{3.2}$$

where y^{exp} are the values from the Gaussian fit, n is the number of data points and p is the number of parameters fitted. For a two Gaussian fit $p = 6$, and for a four Gaussian fit $p = 12$. The ^{13}CO fit showed a $\chi^2_{red} = 0.151$. The C^{18}O fit showed a $\chi^2_{red} = 0.010$.

3.2.3 Integrated Intensity Maps toward the IRDC and GMC

To map the velocity components of the IRDC, integrated intensity maps were constructed based on the velocity analysis explored in the previous section. The concept of such a map is essentially to flatten a 3-dimensional dataset into a 2-dimensional image. This was done by integrating the brightness temperature over a determined velocity range. This returns a single value for the integrated brightness temperature in K km s^{-1}. Repeating this for all the pixels and displaying the image results in a map that shows how the emissions corresponding to the velocity range are distributed. This was done only for the 1-0 transition of ^{13}CO since it is the best tracer for the IRDCs structure and its kinematics (as explained in Section 1.4).

The integrated intensity map from the ^{13}CO data is shown in Figure 3.3 to the right. The map is shown for the whole IRDC and has been integrated over the velocity peak centered at 53 kms^{-1}. The integrated intensity map is shown together with the mass surface density map on the left. Contours from the integrated intensity map have been overlaid on the mass surface density map in order to relate the two. A third plot with contours from the mass surface density map overlaid on the integrated intensity map is shown on the bottom in Figure 3.3. The contours aim to show the outline of the IRDC.

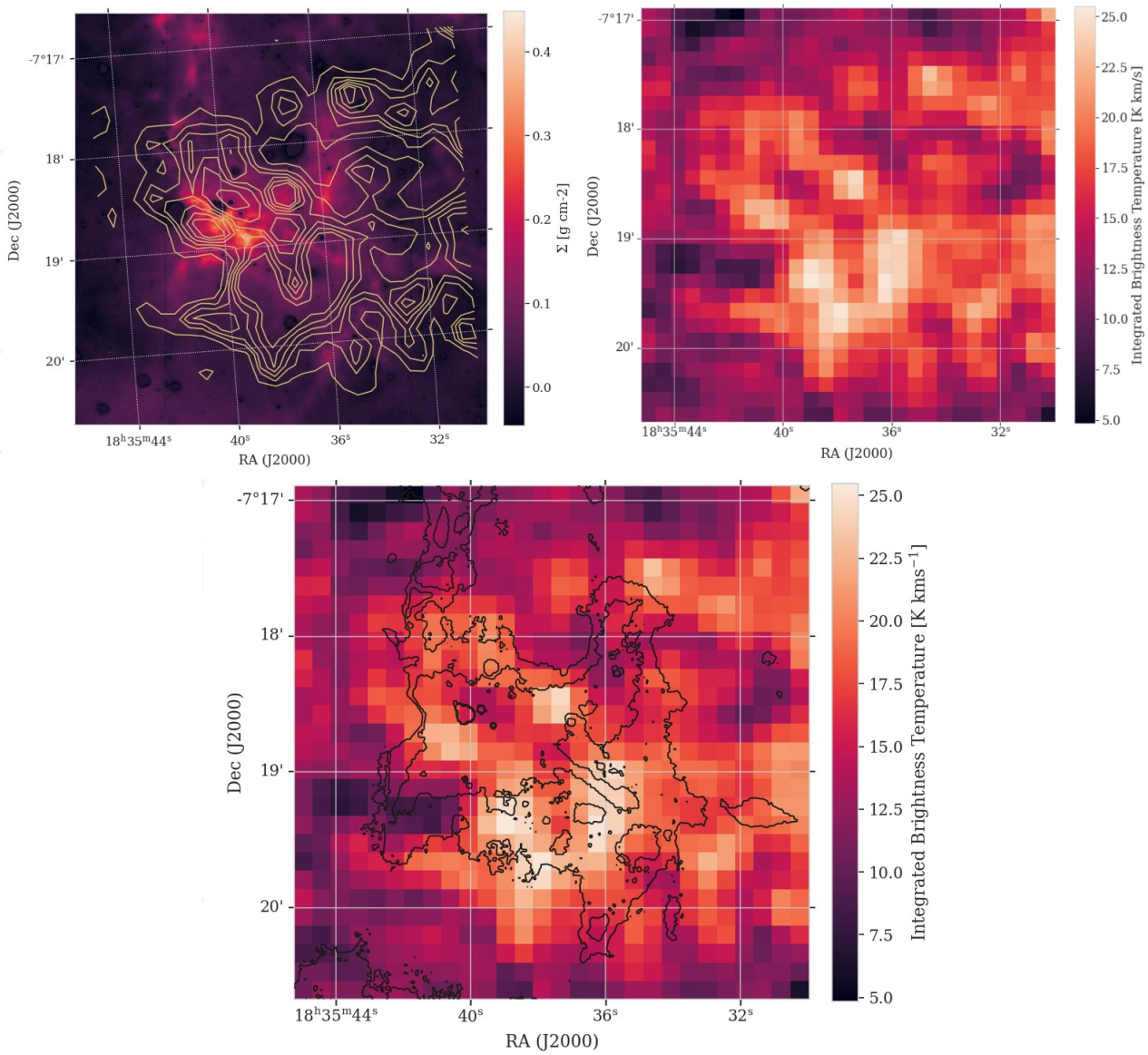

Figure 3.3: *Right*: The integrated ^{13}CO intensity map for the IRDC G024.64+00.16. The map is integrated over the velocity range 49.5-57.3 km s^{-1}, which encompasses the peak at 53 km s^{-1}. *Left*: the contours from the integrated intensity map overlaid on the mass surface density map. The yellow contours are shown for 60% - 85% of the total intensity. *Bottom*: the integrated intensity map with black contours from the mass surface density map at $\Sigma = 0.05, 0.09$ g cm^{-2} overlaid.

The integrated intensity map shows two parallel filaments. In Figure 3.4 two additional integrated intensity maps are shown. The two velocity maps are based on the two velocity components from the peak at 53 km s^{-1} in Figure 3.2.

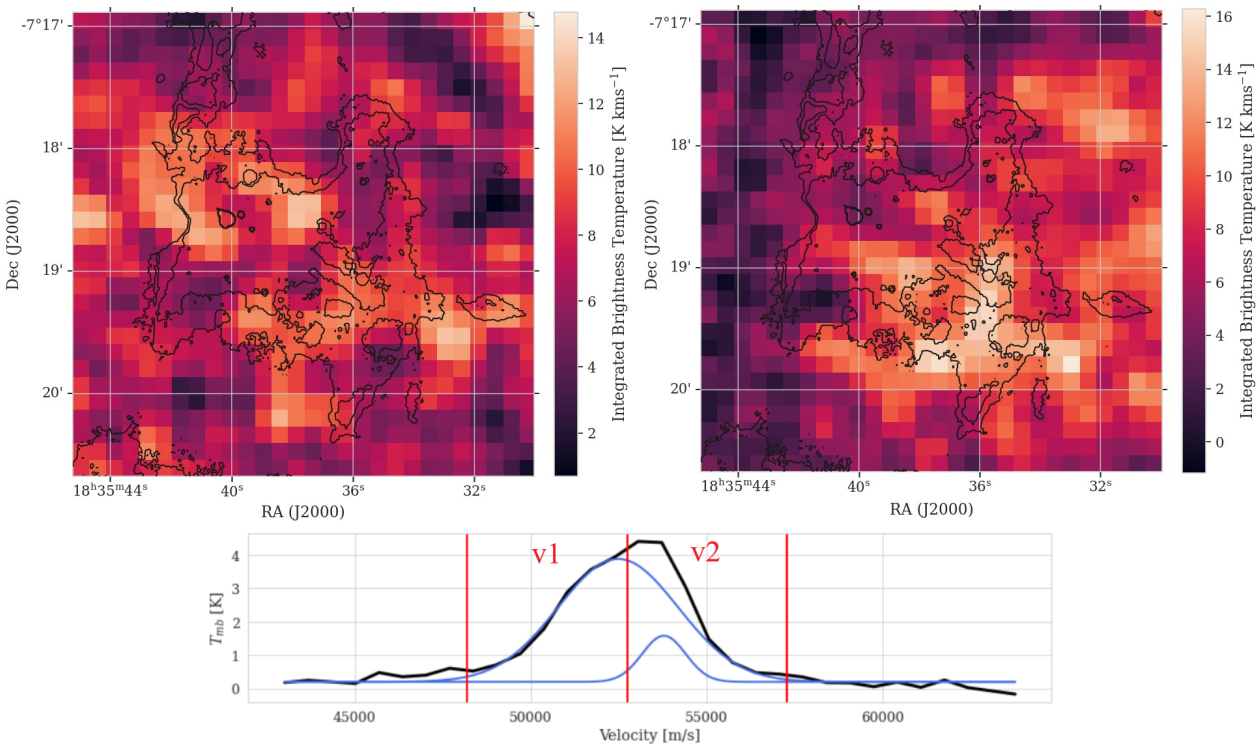

Figure 3.4: *Left*: integrated intensity map that has been integrated over the velocity range 48.2-52.7 $\mathrm{km\,s^{-1}}$ (v1). *Right*: similarly to the left, but having been integrated over the velocity range 52.7-57.3 $\mathrm{km\,s^{-1}}$ (v2). The maps also contain black contours from the mass surface density map at $\Sigma = 0.05, 0.09$ g $\mathrm{cm^{-2}}$.

The map on the left has been integrated over the range 48.2-52.7 $\mathrm{km\,s^{-1}}$ (v1) shown on the spectrum at the bottom, and similarly for the right map but over the range, 52.7-57.3 $\mathrm{km\,s^{-1}}$ (v2). The integrated intensity map for v2 seems to be concentrated below and to the right of where the mass is centered (see Figure 3.3), while the the map corresponding to v1 is evenly distributed around the cores.

Maps of the surrounding GMC were also created, integrated over the velocity peaks of the ^{13}CO spectrum identified in Figure 3.1. This was done in order to determine the position of these velocity components within the GMC. Figure 3.5 shows the integrated intensity map over the peak at 53 $\mathrm{km\,s^{-1}}$ (49.5 - 57.3 $\mathrm{km\,s^{-1}}$). The location of IRDC G024.64+00.16 is marked with a yellow circle.

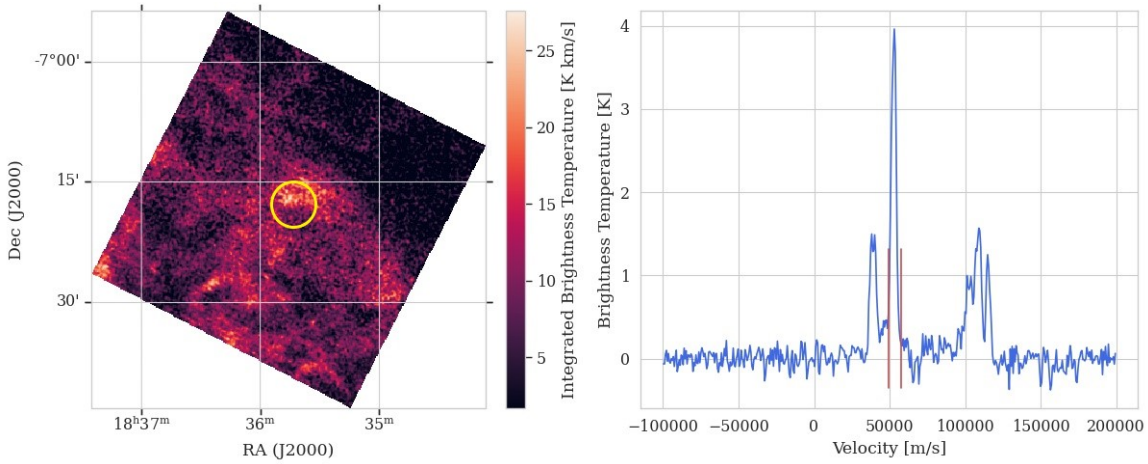

Figure 3.5: On the left is the integrated intensity map of the ^{13}CO integrated over 49.5-57.3 kms^{-1}. The map encompasses the entire data set.

Figure 3.5 shows the integrated intensity map (on the left) and integration interval (on the right) marked with red lines. The map shows that both the IRDC and large parts of the GMC is moving at this velocity, which is expected as the mean velocity of the IRDC is 51.3 kms^{-1}. Figure 3.6 shows the same region as Figure 3.5 integrated over the peak at 40 kms^{-1} (34.6-43.7 km s^{-1}). The IRDC's location is marked with a yellow circle.

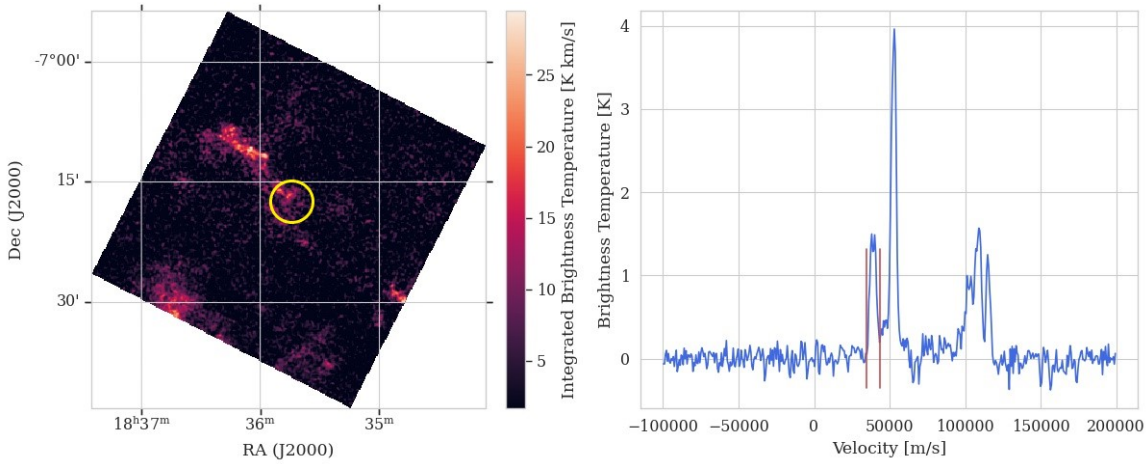

Figure 3.6: The integrated intensity map of the ^{13}CO data is displayed on the left, integrated over 34.6-43.7 km s^{-1}. IRDC G024.64+00.16 is located within the yellow circle. To the right is the entire ^{13}CO spectrum with the integration interval marked with red lines.

Figure 3.6 shows that the structure moving at 40 km s^{-1} which seems mostly unrelated to the IRDC. There seems however to be something within the IRDC which moves at this velocity, this is discussed further in Section 5.3. Figure 3.7 shows the map of the surrounding GMC integrated over the peaks at 110 km s^{-1} (100.9-118.9 km s^{-1}).

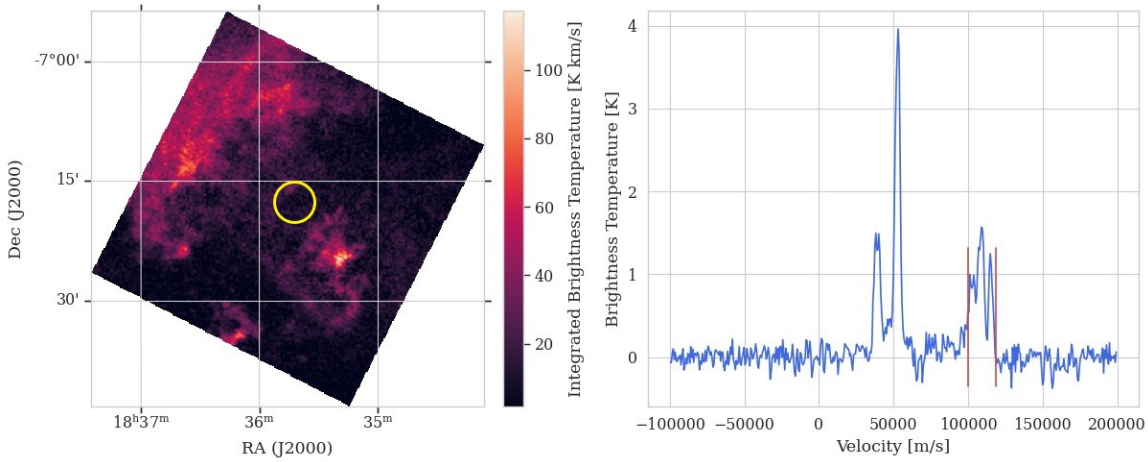

Figure 3.7: The integrated intensity map of the ^{13}CO data is displayed on the left, integrated over 100.9-118.9 kms^{-1}. IRDC G024.64+00.16 is located within the yellow circle. To the right is the entire ^{13}CO spectrum with the integration interval marked with red lines.

Figure 3.7 shows that the structures moving at 110 km s^{-1} seems to be unrelated to the IRDC.

3.3 Kinematic Analysis of the Cores

We present a similar analysis as the one from Section 3.2.2 for the six cores identified in Section 2.3. These cores are divided into regions based on the angular resolution of the CO data.

Since the CO data is taken at an angular resolution of 20″, the diameter of the extracted regions can be no less than this. This means that the the regions for which the CO data was extracted is bigger than the contours of the cores in Figure 2.3. From here on forth, results will be based on the three constructed regions shown in Figure 3.8 as green circles, instead of the six cores previously identified. Region 1 includes only core 3, region 2 includes cores 5 and 6. These are 20″ in diameter. Region 3 includes cores 1, 2 and 4, and is 30″ in diameter. Due to the angular resolution of 20″ it was impossible to separate the cores further. Only cores 3, 5 and 6 were deemed to be separate cores belonging to the IRDC. This is discussed further in Section 5.1.

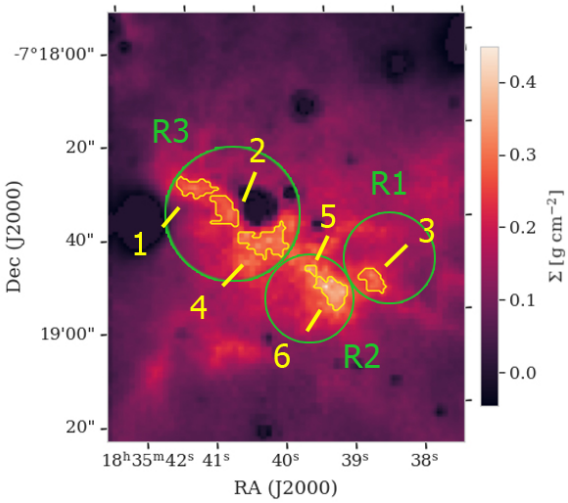

Figure 3.8: Mass surface density for the IRDC G024.64+00.16. The three regions are marked as green circles on the mass surface density map. Region 1 and 2 have a diameter of 20″, the same size as the beam. Region 3 has a diameter of 30″.

The extracted ^{13}CO spectra, centered on the main spectral peak of 53 kms^{-1} for regions 1, 2 and 3 are shown in Figure 3.9 together with a two Gaussian fit to the peaks. The Gaussian fits showed a $\chi^2_{red} = 0.111, 0.391$ and 0.519 for regions 1, 2 and 3 respectively.

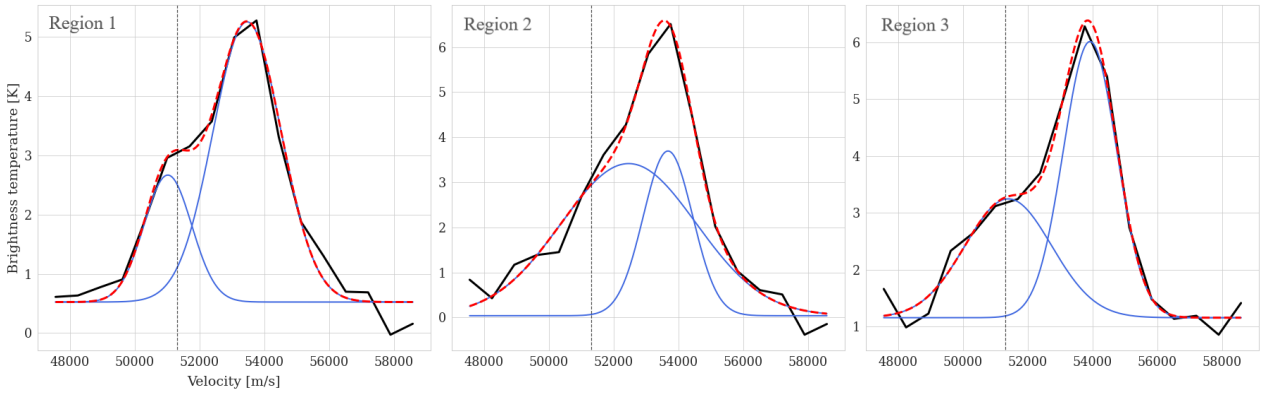

Figure 3.9: Two Gaussian fitting to the extracted spectra for region 1 (left), region 2 (middle) and region 3 (right). The ^{13}CO data is shown in black, the Gaussian fitting is shown in red whereas the individual components are shown in blue. The spectra are shown for a small range centered around the main spectral peak of 53 kms^{-1}. The multi-Gaussian fits showed a $\chi^2_{red} = 0.111, 0.391$ and 0.519 respectively. The cloud's velocity is marked as a gray dashed line at 51.3 km s^{-1}.

Region 1 in Figure 3.9 shows two clear Gaussian components making up the spectral peak. For region 2 this is less noticeable with the peak composed of one wide and one narrow Gaussian of similar amplitude. Region 3 shows two distinct Gaussian components, one making up the peak and one off to the side with about half the amplitude of the first one. The peaks of all regions are moving at a higher velocity than the IRDC's mean velocity of 51.3 km s^{-1}, marked as a gray dashed line.

The extracted C^{18}O spectra for region 1, 2 and 3 did not meet the requirement in terms of noise according to Section 3.2.1 and were thus not fitted to any Gaussian functions. Their spectra are however presented in Figure A2 in the Appendix.

3.4 Conclusions from the Kinematic Analysis

We have found three velocity peaks in the ^{13}CO spectrum. These peaks were located at 40 km s^{-1}, 53 km s^{-1} and 110 km s^{-1}. The peaks at 40 km s^{-1} and 110 km s^{-1} seems to be unrelated to the IRDC. The C^{18}O spectra showed one velocity peak at 53 km s^{-1}. The velocity spectra for each of the surveyed regions yielded asymmetric distributions moving at higher velocities than the IRDC's mean velocity. The integrated intensity maps showed an intensity minimum at the location of the suspected cores. This region is situated between two filaments of intensity maxima.

4 Physical Conditions of the Molecular Gas in the IRDC G024.64+00.16

The physical conditions of the gas in the cloud can give us crucial information about the environment massive stars are formed in. By calculating physical conditions of the cores such as the column density, depletion factor and performing a virial analysis on the identified cores, we aim to obtain further understanding on the previously identified massive cores. In this Chapter, we estimate the ^{13}CO and C^{18}O column density, depletion factor and virial parameter for the IRDCs and toward the regions described in Chapter 3.

4.1 Calculating the Column Density

The column density, N(^{13}CO) and N(C^{18}O), is defined as the number of atoms per unit area of a defined region between an observer and the astronomical object of interest (Mangum & Shirley 2015). When using the molecular spectral line measurements to calculate the column density, it will result in the column density involving the radiative transfer properties of the molecular spectral line. As described in Mangum & Shirley (2015), the column density of a molecule can be derived by the following equation:

$$N_{tot} = \frac{8\pi\nu^3}{Ag_{ul}c^3}\left(\frac{k}{h\nu}\right)\frac{1}{J_v\left(T_{ex}\right)-J_v\left(T_{bkg}\right)}\frac{Q_{rot}}{1-\exp\left(\frac{-h\nu}{kT_{ex}}\right)}\frac{1}{\exp\left(\frac{-E_{low}}{kT_{ex}}\right)}\int T_{mb}dV \tag{4.1}$$

where ν is the rest frequency of the molecule, A is the Einstein coefficient, g_{ul} is the degeneracy of the upper energy level and c is the speed of light. In our case it is the rotational degeneracy given by $g_u = 2J+1$, where J is the rotational quantum number. k is the Boltzmann constant and h is the Plank constant. $J_v(T)$ is the Plank function, T_{bkg} is the background temperature, T_{ex} is the excitation temperature, E_{low} is the energy of the lower state and Q_{rot} is the rotational partition function. The values of E_{low} and A for the transition of CO were taken from the online catalogue *splatalogue* (Markwick-Kemper et al. 2006). T_{mb} was obtained from the extracted spectra in Section 3.2.1. Q_{rot} can be calculated from

$$Q_{rot} = \sum_{J=0}^{\infty}(2J+1)exp(\frac{-E_J}{kT}) \tag{4.2}$$

where E_J is the energy in state J given by $E_J = J(J+1)hB$, and B is the rotational constant. This leaves us with one equation and two unknown variables, N_{tot} and T_{ex}. Therefore, a value for T_{ex} needs to be assumed in order to obtain N_{tot}. Because of the low quantum state of the CO, we assume a low value of $T_{ex} = 7.5$ K and calculate N_{tot} as described by Hernandez et al. (2011). To make an estimate of the error we calculated N_{tot} for $T_{ex} = 4.5$ K, 15 K and compare

these values with the one for 7.5 K to get an estimation of how much the value of N_{tot} change with the assumption of different temperatures.

The different values of the ^{13}CO column densities obtained from varying T_{ex} in Equation 4.1 is shown in Table 4.1.

Table 4.1: The ^{13}CO column density calculated for varying T_{ex} in Equation 4.1.

	^{13}CO Column density (10^{16} cm^{-2})		
	$T_{ex} = 4.5K$	$T_{ex} = 7.5K$	$T_{ex} = 15K$
Region 1	2.583	1.8655	2.199
Region 2	2.890	2.0873	2.461
Region 3	3.157	2.281	2.689
IRDC	2.116	1.528	1.802

Increasing the excitation temperature to 15 K results in a 17.9 % increase in the column density for the IRDC. Decreasing the excitation temperature to 4.5 K increases the column density for the IRDC with 38.5%. Since the method is similar, the C^{18}O column densities were only calculated for $T_{ex} = 7.5$K. All column densities at $T_{ex} = 7.5$K are shown in Table 4.2

4.2 CO Depletion

The depletion factor tells us the fraction of CO that is frozen onto dust in the IRDC by comparing the expected and observed abundances (Hernandez et al. 2011). The CO depletion factor is defined as

$$f_D = \frac{\chi(\mathrm{CO})^{\mathrm{expected}}}{\chi(\mathrm{CO})^{\mathrm{observed}}} \tag{4.3}$$

where χ(CO) is the molecular abundance defined as

$$\chi(\mathrm{CO}) = \frac{N(\mathrm{CO})}{N(\mathrm{H_2})} \tag{4.4}$$

As presented by Hernandez et al. (2011), the depletion factor can be calculated by comparing the CO mass surface density, Σ_{CO}, with the small median filter (SMF: a digital filtering technique), mid-infrared extinction mapping derived mass surface density map Σ_{SMF} by

$$f_D = \frac{\Sigma_{\mathrm{SMF}}}{\Sigma_{\mathrm{CO}}} \tag{4.5}$$

Σ_{SMF} can be obtained from extracting the mass surface density from a region in the map used in Chapter 2. This leaves Σ_{CO} to be calculated. We present below the method of obtaining a mass surface density from ^{13}CO by applying a similar method to that shown in Hernandez

et al. (2011). The relation between column density and mass surface density is (Jiménez-Serra et al. 2014)

$$\Sigma_{13\mathrm{CO}} = \frac{1}{\chi(^{13}\mathrm{CO})} m(\mathrm{H_2}) \mathrm{N}(^{13}\mathrm{CO}) \tag{4.6}$$

where $m(\mathrm{H_2})$ is the mass of the hydrogen molecule and $N(^{13}\mathrm{CO})$ is the $^{13}\mathrm{CO}$ column density. We assume that the CO molecular abundance in the ISM is $\chi(\mathrm{CO}) = 2\times10^{-4}$ (Lacy et al. 1994). The abundance of $^{12}\mathrm{CO}$ to $^{13}\mathrm{CO}$ changes in individual objects and can vary quite substantially. Wilson & Rood (1994) presents the value

$$\frac{^{12}\mathrm{C}}{^{13}\mathrm{C}} = 53 \tag{4.7}$$

which leads to $\chi(^{13}\mathrm{CO}) = 4.53 \times 10^{-6}$. We have that the mass of hydrogen is 3.32×10^{-24} g, added to this we have a 40 % contribution from helium. This results in a final value for the mass of hydrogen, $m(\mathrm{H_2})$= 4.68×10^{-24} g. By dividing and scaling it to 10^{16} we obtain the final relation

$$\Sigma_{13CO} = 1.24 \times 10^{-2} \left(\frac{N(^{13}\mathrm{CO})}{10^{16}} \right) \tag{4.8}$$

Similarly for $\mathrm{C^{18}O}$, Hernandez et al. (2011) arrives at the relation

$$\Sigma_{C18O} = 7.652 \times 10^{-2} \left(\frac{N(\mathrm{C^{18}C})}{10^{16}} \right) \tag{4.9}$$

When looking at star forming regions we expect the depletion factor to be >1 (Lewis et al. 2021) since this suggests that the temperature at the core is less than the freezing point of CO and that the core is very dense (Hernandez et al. 2011).

Table 4.2 presents the calculated column density and mass surface density for region 1, 2 and 3 and the entire IRDC from the $^{13}\mathrm{CO}$ and $\mathrm{C^{18}O}$ data. The table also presents the depletion factor for both CO isotopologues.

Table 4.2: The column density and surface density for the two regions and the whole IRDC together with their respective depletion factor. Calculations are shown for both $^{13}\mathrm{CO}$ and $\mathrm{C^{18}O}$.

	N(^{13}CO) (10^{16} cm^{-2})	Σ_{13CO} (g cm^{-2})	$f_D(^{13}\mathrm{CO})$	N($\mathrm{C^{18}O}$) (10^{16} cm^{-2})	Σ_{C18O} (g cm^{-2})	$f_D(\mathrm{C^{18}O})$
Region 1	1.8655	0.0231	10.13	0.4963	0.0379	6.41
Region 2	2.0873	0.0258	9.06	0.6525	0.0499	4.88
Region 3	2.2806	0.0283	6.15	0.8126	0.0622	2.80
IRDC	1.5282	0.0190	-	0.4523	0.0346	-

As shown in Table 4.2, all regions show an $f_D > 1$. This indicates that the temperature is sufficiently low and the density sufficiently high in all regions for CO to freeze out onto the dust grains.

4.3 Virial Analysis

The viral theorem is used to estimate if the gas of a core is gravitationally bound or unbound. This is done by comparing the gravitational potential energy with the kinetic energy. For particles bound together in a system at equilibrium the following holds

$$2K + U = 0 \tag{4.10}$$

where K is the kinetic energy of the particles and U is the gravitational potential energy (Kauffmann et al. 2013). We assume that these are the only sources of energy and that the core is spherical. Applying the viral theorem we have that

$$\frac{2K}{\mid U \mid} = 1 \tag{4.11}$$

when the core is in equilibrium. For a core not in equilibrium, we introduce the virial parameter $\alpha_{vir} = 2K/|U|$ (Bertoldi & McKee 1992). When $\alpha_{vir} \geq 1$ the core has enough kinetic energy to expand and disperse, the core is said to be gravitationally unbound. When $\alpha_{vir} < 1$ the core does not have enough kinetic energy and will collapse. The core is then said to be gravitationally bound. For a spherical core we have that the gravitational energy is given by

$$U = \frac{-3}{5}\frac{GM^2}{R} \tag{4.12}$$

and the kinetic energy as

$$K = \frac{3}{2}V\rho\sigma^2 = \frac{3}{2}M\sigma^2 \tag{4.13}$$

where R is the radius of the core, M is the mass of the core, G is the gravitational constant and σ the average total one-dimensional velocity dispersion. This gives us the final expression for the virial parameter

$$\alpha_{vir} = \frac{5R\sigma^2}{GM}. \tag{4.14}$$

The mass of each core is calculated by extracting the mean surface density from the surface density map in SAOImageDS9 and then multiplying with the area of the beam. The radius of the core can be calculated trigonometrically using the distance to the cloud and the resolution of the beam. The velocity dispersion is obtained by fitting a Gaussian to the CO spectral peak similar to what was done in section 3.2.2. The virial parameter was calculated for all cores by applying Equation 4.14.

Table 4.3 presents the calculated α_{vir} for the three regions. The table also presents the variables applied to Equation 4.14. Σ_{SMF} for a region was obtained from the same map used

in Section 2. The mass, M, was obtained by multiplying $\Sigma_{\rm SMF}$ with the area of the region, obtained from the angular resolution and distance to the IRDC. σ was obtained from a one Gaussian fit to the brightest peak of the corresponding region shown in Figure 3.9. This value is discussed further in Section 5.5.

Table 4.3: The values used in the virial analysis and the resulting virial parameter. The mass surface density, $\Sigma_{\rm SMF}$, was obtained with SAOImageDS9. The average total velocity dispersion, σ, was obtained by performing a one Gaussian fit to the spectral peaks for region 1, 2 and 3 in Figure 3.9.

	$\Sigma_{\rm SMF}$	M	σ	α_{vir}
	(g cm^{-2})	(M$_\odot$)	(km s^{-1})	
Region 1	0.180	70.99	1.715	7.78
Region 2	0.235	92.40	1.423	4.11
Region 3	0.174	70.04	1.239	4.20

Every region contain a mass of 70-100 M$_\odot$ which is more than enough to create massive stars (e.g. Tan et al. 2014, Beuther et al. 2007). The virial parameter for each region does however suggest that none of the regions are gravitationally bound Chevance et al. (2020).

4.4 Conclusions about the Physical Conditions

We find that the calculated column densities for both ^{13}CO and C^{18}O are in agreement with those found in similar IRDCs (e.g. Liu et al. 2014, Jiménez-Serra et al. 2014). We show signs of both ^{13}CO and C^{18}O depletion in the three regions studied and the values for f_D are consistent with those found in star forming regions (Pon et al. 2016, Hernandez et al. 2011). We find $\alpha_{vir} > 1$ for all three regions which implies that the cores are not gravitationally bound.

5 Discussion

The results obtained in this study are based on various assumptions and uncertainties. In this Chapter, we discuss in more details our results and comment on improvements and future work that could be followed-up.

5.1 Core Selection and Validity

When searching for the presence of massive cores within the IRDC we investigated a mass surface density map with the help of a dendrogram. The dendrogram resulted in six possible cores. We can see from Figure 2.3 that cores 2 and 4 are in close proximity of a dark region between us and the IRDC, they also seem to trace their silhouette. From images C) and D) in Figure 2.4 we see that the cores are likely part of the emissions from these obstructing objects. We therefore find it highly probable that these cores are not themselves cores but in fact artifacts from the field stars. The most likely explanation is that the dendrogram algorithm picked out the wings of the point spread function (PSF) of the dark object. The PSF characterizes the distortion of the observed light distribution (Ngolè Mboula et al. 2015). As for core 1, it lies in between two point-like signatures, and due to uncertainty we consider this core also as an spurious detection and it is therefore discarded. For these reasons we will not discuss these cores further.

As for core 3, 5 and 6, these remained largely unchanged when the dendrogram parameters were changed. Therefore, we find it likely that these are real cores and not artifacts. The close proximity of cores 5 and 6 and the relatively high mass surrounding them could indicate that fragmentation has occurred during the collapse of this region, leaving a cluster of smaller cores. Image A) in Figure 2.4 indicates the possibility of a smaller core having formed in the vicinity of core 6 which could also indicate fragmentation. In order to investigate whether fragmentation has occurred, the IRDC needs to be examined at higher resolution (Henshaw et al. 2016), thus motivating future work in this direction.

5.2 Core Emissions

Figure 2.4 indicates none of the cores 3, 5 or 6 emit light at any of the surveyed wavelengths. This suggests that these cores could be starless. This subject should however be further researched since only 4 different wavelengths were surveyed. It could be that the cores emit a wavelength not surveyed in this report. There are however kinematic signs of outflows, such as asymmetric velocity distributions, which would indicate that the cores are in fact in an early protostellar stage and not starless. This will be discussed further in Section 5.3.

Because of the limited angular resolution of the images in Figure 2.4, we cannot distinguish objects with a small angular separation. When looking at the cores in these images we see that two of the cores lay close to an object that probably is located somewhere between us and the IRDC, this could be due to a projection effect. Therefore the potential emissions of these cores

becomes blocked by the stronger emissions of this object. With a higher resolution it would be possible to gain more information about these cores. It would also be possible to separate cores 5 and 6.

5.3 Kinematics

We extracted the ^{13}CO and C^{18}O spectra for the entire IRDC and and fitted Gaussian functions to the relevant velocity peak. The relevancy of the velocity peaks of the entire IRDC were determined through integrated intensity maps, these were also used to determine the distribution of the moving mass within the IRDC. We will first discuss the ^{13}CO spectrum from Figure 3.1. Besides the main peak at 53 km s^{-1}, the spectrum shows several other peaks located at 40 km s^{-1} and 110 km s^{-1}. When looking at the integrated intensity maps of the GMC corresponding to these velocities (see Figures 3.6 and 3.7), it can be observed that the emissions at are not strongest where the IRDC is located. The emissions in Figure 3.6 seem to belong to a thin filamentary structure that does show some emissions in the IRDC, however the structure is moving at a different speed and its emissions are relatively weak. We can not conclude whether this structure is part of the IRDC or not. The emissions corresponding to the peaks at 110 km s^{-1} (Figure 3.7) are clearly located outside the boundaries of the IRDC. It can therefore be said that the emissions at the corresponding velocities do not belong to the IRDC.

Panel A) of Figure 2.4 indicates a lack of 4.5 µm emissions suggesting that there are no outflows. However, Figure 3.9 shows that the peak is moving at a higher speed than the mean velocity of the cloud as well as with an asymmetric velocity distribution, which are signs of outflow motion according to Zhou et al. (2019) and Pillai et al. (2019). The same can be seen for the C^{18}O spectrum shown in Figure 3.2. In order to further explore the existence of an outflow, observations taken at a higher resolution should be analyzed. Focusing on more appropriate tracers for outflow such as SiO and ^{12}CO (Miettinen 2012) should also be considered. Higher resolution data would allow for the possibility of zooming in on separate cores which would provide a more accurate spectrum. These observations could show more distinct evidence for outflow activity for the cores, in a similar fashion to those found in Liu et al. (2014).

Due to the low signal-to-noise ratio, it was not possible to do a Gaussian fitting for the extracted C^{18}O spectra for regions 1, 2 and 3. The peaks at the relevant velocity did not meet the criteria for peak certainty according to Section 3.2.1. The spectra for regions 1, 2 and 3 are shown in Figure A2 in Appendix, but are not further discussed.

Figure A1 suggests that the IRDC is situated in the middle of a GMC or possibly in between two GMCs. This could indicate that the IRDC could have been formed as a result of these two GMCs colliding. Figure 3.6 shows that there might be some component of the IRDC moving at 40 km s^{-1}. If this is the case it could be sign of cloud-cloud collision (Fukui et al. 2013). It should be noted that the structure moving at this velocity could also be part of some object between us and the IRDC. The spectra for the whole IRDC, shown in Figure 3.1 does however not show any similarities to those presented by Hernandez & Tan (2015) and Wu et al. (2017), suggesting that the IRDC has not formed as a result of cloud-cloud collision. This could be further investigated by a postion-velocity analysis as presented by Hernandez & Tan (2015). Additionally, observations targeting the SiO line could be investigated, as this tracer could be

enhanced in shock regions (Cosentino et al. 2019).

5.4 Column Density and Depletion

As stated in Section 4.4, the calculated column densities for both ^{13}CO and C^{18}O are in agreement with those found in similar IRDCs. While the order of magnitude does agree, the exact value obtained does include some uncertainties. When calculating the column density from the method presented by Mangum & Shirley (2015), an excitation temperature needs to be assumed. This excitation temperature describes the energy density of all kinds of energy for the different molecules as a general energy. It also assumes that the energy is the same for all transitions, although most molecules have different excitation temperature for different transitions. Assuming a value of T_{ex} leads to a value of N_{tot} that might not be correct. In the interval 4K to 15K there is an difference in N_{tot} of up to 38.5% from the assumed T_{ex}. Table 4.1 indicates a steeper change in column density when the excitation temperature is decreased than when it is increased. We can conclude that our obtained column densities does include some uncertainties due to error within the same order of magnitude.

The method used to obtain f_D is based on knowing the column density. Hence, the values for f_D discussed below are subject to the same level of uncertainty as the column density. With that in mind, our obtained values of $f_D(^{13}\text{CO}) = 10.13$, 9.06 and 6.15 for region 1, 2 and 3 respectively are within the bounds of those presented by Pon et al. (2016) for star forming regions. The values we obtained for $f_D(\text{C}^{18}\text{O})$ are in accordance with those presented by Hernandez et al. (2011) for massive protostellar cores. These results suggest that within the regions analyzed, the conditions are sufficiently cold and dense for the formation of massive cores to occur.

The integrated intensity maps, shown in Figure 3.3, show an emission minimum in the areas in and around cores 3, 5 and 6 which is in agreement with Miettinen (2012), further suggesting that these areas have high depletion of ^{13}CO.

5.5 Virial analysis

We calculated the virial parameter α_{vir} in order to determine whether the gas in the surveyed regions is gravitationally bound or not. The virial parameter is only a rough estimate and contains a number of reasonable assumptions in order to arrive at Equation 4.14. These include the assumption of a perfect sphere with a homogeneous distribution of its mass. We used some basic trigonometry and the distance to the cloud in order to calculate the radius of the core. Different method used to calculate the distance to the cloud gives different results (Kauffmann et al. 2013) leading to variations in the results for the virial parameter of a factor of up to 2. The methods used when calculating the properties affect the results which is clear when comparing the results from Heyer et al. (2009) and Roman-Duval et al. (2010). Both studies build on the same set of observations, but the method used to extract the cloud structure differs and leads to different results when calculating the virial parameter. The method used by Roman-Duval et al. (2010) is suited for calculating α_{vir} while our method is simpler. Since the results for α_{vir} are not $\ll 1$ it is hard to tell how big of an impact the assumption of a perfect sphere has on

the results.

Ignoring the assumptions made, the final equation itself has uncertainties that contribute to the parameter. The velocity dispersion, σ, was obtained by fitting a one Gaussian to the peaks shown in Figure 3.9. This method of obtaining a total velocity dispersion is not exact since we end up using one function where at least two are required for a good fit, however, a good estimate could still be retrieved. This has the possibility of resulting in a larger σ due to several velocity components needing to be over-fitted. Due to α_{vir} having a squared σ dependence, this further amplifies the error. Another method of obtaining σ is mentioned in Barnes et al. (2021) where they assign the velocity component with the largest integrated intensity to the core and from there, obtain the corresponding σ. This avoids over-fitting the spectrum, however one needs to verify that the biggest velocity component actually is the one belonging to the core. Barnes et al. (2021) performs a manual check by constructing an integrated intensity map of the individual velocity components and then comparing the maxima to the locations of the cores. If a velocity component does belong to a core, one would expect to see the global maxima within the contour of the core. This method is more reliably applied when the core shows clear separation of the velocity components. From our results, region 2 shows two velocity components not strongly separated. Regions 1 and 3 however have two velocity components that are separated, and hence could be subject to further analysis with the method used in Barnes et al. (2021) but was out of the scope of this study. It is, nonetheless, another avenue to explore in future work.

The virial parameter for regions 1, 2 and 3 were >1 for both ^{13}CO and C^{18}O. This suggests that the cores are gravitationally unbound or that the regions could be confined by external pressure according to Chevance et al. (2020). As discussed above, this result is not entirely reliable, and an exact measure of the error is hard to obtain. Previous results would indicate the possibility of the cores being in the process of forming or having formed which would necessitate the cores being gravitationally bound.

6 Conclusions

To investigate the formation of massive stars in the IRDC G024.64+00.16 we analyzed images taken by the Spitzer Space Telescope and Hershel Space Observatory, as well as CO(1-0) data from the FUGIN survey. The main findings are summarized below.

1. With a mass surface density map, six cores were identified in the IRDC. Three of these cores are thought to be actual cores belonging to the IRDC. The other three cores are most likely best explained as artifacts doe too the PSF of nearby stars. None of the actual cores emit light at the surveyed wavelengths: 4.5, 8, 24 and 70 µm. This suggests that they could be starless or in the early stages of their evolution.

2. For the kinematic analysis, the cores were divided into three regions. The velocity spectra for all three regions showed signs of outflows. The velocity spectrum from the entire IRDC showed some signs of cloud-cloud collision. These findings were however inconclusive.

3. The column density calculations resulted in values typical for IRDCs. N(^{13}CO) for the two most promising star-forming regions in the IRDC were found to be 1.87 and 2.09 $\times 10^{16}$cm^{-2}. N(C^{18}O) was found to be 0.50 and 0.65 $\times 10^{16}$cm^{-2}. These regions showed signs of high CO depletion with $f_D(^{13}\mathrm{CO}) = 10.13$, 9.06 and $f_D(\mathrm{C}^{18}\mathrm{O}) = 6.41$, 4.88.

4. The virial parameter for the promising star-forming regions were 7.78 and 4.11. Regions with a virial parameter $\alpha_{vir} > 1$ are considered to be gravitationally unbound, a criteria met by both regions. However, the method used in obtaining α_{vir} includes many assumptions, and the result can vary by more than a factor of 2.

Acknowledgements

We would like to thank our supervisors Dr. Giuliana Cosentino, Dr. Rubén Fedriani and Dr. Prasanta Gorai for their dedication to the project. Without them, this thesis would not be possible!

References

Barnes, A. T., Henshaw, J. D., Fontani, F., et al. 2021, MNRAS, 503, 4601, doi: 10.1093/mnras/stab803

Bertoldi, F., & McKee, C. F. 1992, ApJ, 395, 140, doi: 10.1086/171638

Beuther, H., Churchwell, E., McKee, C., & Tan, J. 2007, in Protostars Planets V, ed. B. Reipurth, D. Jewitt, & K. Keil, 165. https://arxiv.org/abs/astro-ph/0602012

Bonnarel, F., Ziaeepour, H., Bartlett, J. G., et al. 1998, IAU, 179, 469, doi: 10.1017/S007418090012933X

Butler, M. J., & Tan, J. C. 2009, ApJ, 696, 484, doi: 10.1088/0004-637X/696/1/484

Carroll, B. W., & Ostlie, D. A. 2014, An Introduction to Modern Astrophysics, 2nd edn. (Harlow, UK: Pearson)

Cheng, Y., Tan, J. C., Liu, M., et al. 2018, ApJ, 853, 160, doi: 10.3847/1538-4357/aaa3f1

Chevance, M., Kruijssen, J. M. D., Vazquez-Semadeni, E., et al. 2020, SSR, 216, 50, doi: 10.1007/s11214-020-00674-x

Chira, R.-A., Beuther, H., Linz, H., et al. 2013, A&A, 552, A40, doi: 10.1051/0004-6361/201219567

Cosentino, G., Jiménez-Serra, I., Caselli, P., et al. 2019, ApJL, 881, L42, doi: 10.3847/2041-8213/ab38c5

Egan, M. P., Shipman, R. F., Price, S. D., et al. 1998, ApJ, 494, L199, doi: 10.1086/311198

Evans II, N. J. 1999, ARA&A, 37, 311, doi: 10.1146/annurev.astro.37.1.311

Fraknoi, A., Morrison, M., & Wolff, S. 2016, Astronomy, 1st edn. (Houston: OpenStax), 798–808Fra. https://openstax.org/details/books/astronomy

Frank, A., Ray, T., Cabrit, S., et al. 2014, in Protostars Planets VI, ed. H. Beuther, R. S. Klessen, C. P. Dullemond, & T. Henning, 451, doi: 10.2458/azu_uapress_9780816531240-ch020

Frost, A. J., Oudmaijer, R. D., de Wit, W. J., & Lumsden, S. L. 2021, A&A, 648, doi: 10.1051/0004-6361/202039748

Fukui, Y., Ohama, A., Hanaoka, N., et al. 2013, ApJ, 780, doi: 10.1088/0004-637X/780/1/36

Goldsmith, P. F., Bergin, E. A., & Lis, D. C. 1997, ApJ, 491, 615, doi: 10.1086/304986

Gutermuth, R. A., & Heyer, M. 2015, AJ, 149, 64, doi: 10.1088/0004-6256/149/2/64

Henshaw, J. D., Caselli, P., Fontani, F., et al. 2016, MNRAS, 463, 146, doi: 10.1093/mnras/stw1794

Hernandez, A., & Tan, J. 2015, ApJ, 809, doi: 10.1088/0004-637X/809/2/154

Hernandez, A. K., Tan, J. C., Caselli, P., et al. 2011, ApJ, 738, 11, doi: 10.1088/0004-637x/738/1/11

Heyer, M., Krawczyk, C., Duval, J., & Jackson, J. M. 2009, ApJ, 699, 1092, doi: 10.1088/0004-637X/699/2/1092

Inutsuka, S.-i., Inoue, T., Iwasaki, K., & Hosokawa, T. 2015, A&A, 580, A49, doi: 10.1051/0004-6361/201425584

Jiménez-Serra, I., Caselli, P., Fontani, F., et al. 2014, MNRAS, 439, 1996, doi: 10.1093/mnras/stu078

Joye, W., & Mandel, E. 2003, in Astronomical Society of the Pacific Conference Series, Vol. 295, Astron. Data Anal. Softw. Syst. XII, ed. H. Payne, R. Jedrzejewski, & R. Hook, 489. https://ui.adsabs.harvard.edu/abs/2003ASPC..295..489J

Kainulainen, J., & Tan, J. C. 2013, A&A, 549, doi: 10.1051/0004-6361/201219526

Kauffmann, J., Pillai, T., & Goldsmith, P. F. 2013, ApJ, 779, 185, doi: 10.1088/0004-637X/779/2/185

Kennicutt, R. C., & Evans, N. J. 2012, ARA&A, 50, 531, doi: 10.1146/annurev-astro-081811-125610

Lacy, J., Knacke, R., Geballe, T., & Tokunaga, A. 1994, ApJL, 428, L69, doi: 10.1086/187395

Larson, R. B. 1969, MNRAS, 145, 271, doi: 10.1093/mnras/145.3.271

Lewis, J. A., Lada, C. J., Bieging, J., et al. 2021, ApJ, 908, 76, doi: 10.3847/1538-4357/abc41f

Liu, X.-L., Wang, J.-J., & Xu, J.-L. 2014, MNRAS, 443, 2264, doi: 10.1093/mnras/stu1268

Luhman, K. L. 2011, ARA&A, 50, 65, doi: 10.1146/annurev-astro-081811-125528

Mangum, J. G., & Shirley, Y. L. 2015, PASP, 127, 266, doi: 10.1086/680323

Markwick-Kemper, A. J., Remijan, A., & Fomalont, E. 2006, in American Astronomical Society Meeting Abstracts, Vol. 208, Am. Astron. Soc. Meet. Abstr. #208, 51.01. https://splatalogue.online/index.php

Miettinen, O. 2012, A&A, 545, doi: 10.1051/0004-6361/201219497

Moser, E., Liu, M., Tan, J. C., et al. 2020, Astrophys. J., 897, 136, doi: 10.3847/1538-4357/ab96c1

Ngolè Mboula, F. M., Starck, J.-L., Ronayette, S., Okumura, K., & Amiaux, J. 2015, A&A, 575, A86, doi: 10.1051/0004-6361/201424167

Nguyên Luong, Q., Motte, F., Hennemann, M., et al. 2011, A&A, 535, doi: 10.1051/0004-6361/201117831

Noriega-Crespo, A., Raga, A., Moro-Martin, A., Flagey, N., & Carey, S. 2014, NJP, 16, doi: 10.1088/1367-2630/16/10/105008

Pillai, T., Kauffmann, J., Zhang, Q., et al. 2019, A&A, 622, A54, doi: 10.1051/0004-6361/201732570

Pon, A., Johnstone, D., Caselli, P., et al. 2016, A&A, 587, doi: 10.1051/0004-6361/201527154

Rathborne, J. M., Jackson, J. M., Chambers, E. T., et al. 2010, ApJ, 715, 310, doi: 10.1088/0004-637x/715/1/310

Ridge, N. A., Wilson, T. L., Megeath, S. T., Allen, L. E., & Myers, P. C. 2003, AJ, 126, 286, doi: 10.1086/375455

Ridpath, I. 2012, A Dictionary of Astronomy, 2nd edn. (Oxford University Press), doi: 10.1093/acref/9780199609055.001.0001

Roman-Duval, J., Jackson, J. M., Heyer, M., Rathborne, J., & Simon, R. 2010, ApJ, 723, 492, doi: 10.1088/0004-637X/723/1/492

Rosen, A. L., Offner, S. S. R., Sadavoy, S. I., et al. 2020, SSR, 216, 62, doi: 10.1007/s11214-020-00688-5

Rosolowsky, E. W., Pineda, J. E., Kauffmann, J., & Goodman, A. A. 2008, ApJ, 679, 1338, doi: 10.1086/587685

Sabatini, G., Giannetti, A., Bovino, S., et al. 2019, MNRAS, 490, 4489, doi: 10.1093/mnras/stz2818

Shore, S. N. 2003, in Encycl. Phys. Sci. Technol., 3rd edn., ed. R. A. B. T. Meyers (New York: Academic Press), 737–747, doi: 10.1016/b0-12-227410-5/00726-2

Tan, J. C., Beltrán, M. T., Caselli, P., et al. 2014, Protostars Planets VI, doi: 10.2458/azu_uapress_9780816531240-ch007

Tasker, E. J., & Tan, J. C. 2009, ApJ, 700, 358, doi: 10.1088/0004-637x/700/1/358

Tielens, A. G. G. M. 2013, Rev. Mod. Phys., 85, 1021, doi: 10.1103/RevModPhys.85.1021

Umemoto, T., Minamidani, T., Kuno, N., et al. 2017, PASJ, 69, doi: 10.1093/pasj/psx061

Vasyunina, T., Linz, H., Henning, T., et al. 2009, A&A, 499, 149, doi: 10.1051/0004-6361/200811226

—. 2011, A&A, 527, doi: 10.1051/0004-6361/201014974

Wilson, T. L., & Rood, R. T. 1994, ARA&A, 32, 191, doi: 10.1146/annurev.aa.32.090194.001203

Wu, B., Tan, J., Christie, D., et al. 2017, ApJ, 841, doi: 10.3847/1538-4357/aa6ffa

Yamamoto, S. 2017, Introduction to Astrochemistry, 1st edn. (Tokyo: Springer), doi: 10.1007/978-4-431-54171-4

Zhou, C., Zhu, M., Yuan, J., et al. 2019, MNRAS, 485, 3334, doi: 10.1093/mnras/stz603

Zinnecker, H., & Yorke, H. W. 2007, ARA&A, 45, 481, doi: 10.1146/annurev.astro.44.051905.092549

Appendix

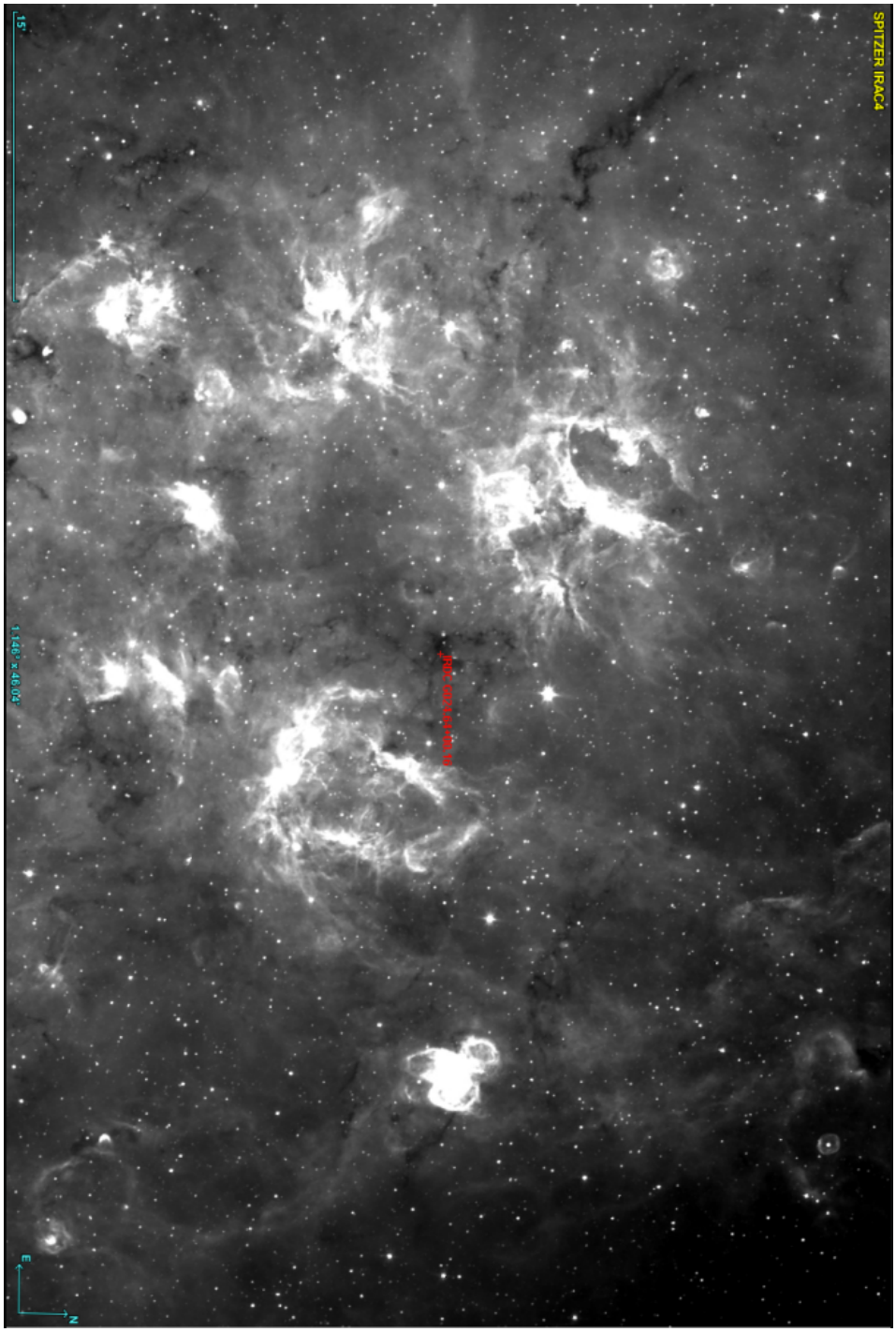

Figure A1: Zoomed out image taken in 8 µm of the IRDC G024.64+00.16 showing the IRDC being situated between GMCs which could be potential evidence of the IRDC forming as a result of cloud-cloud collision.

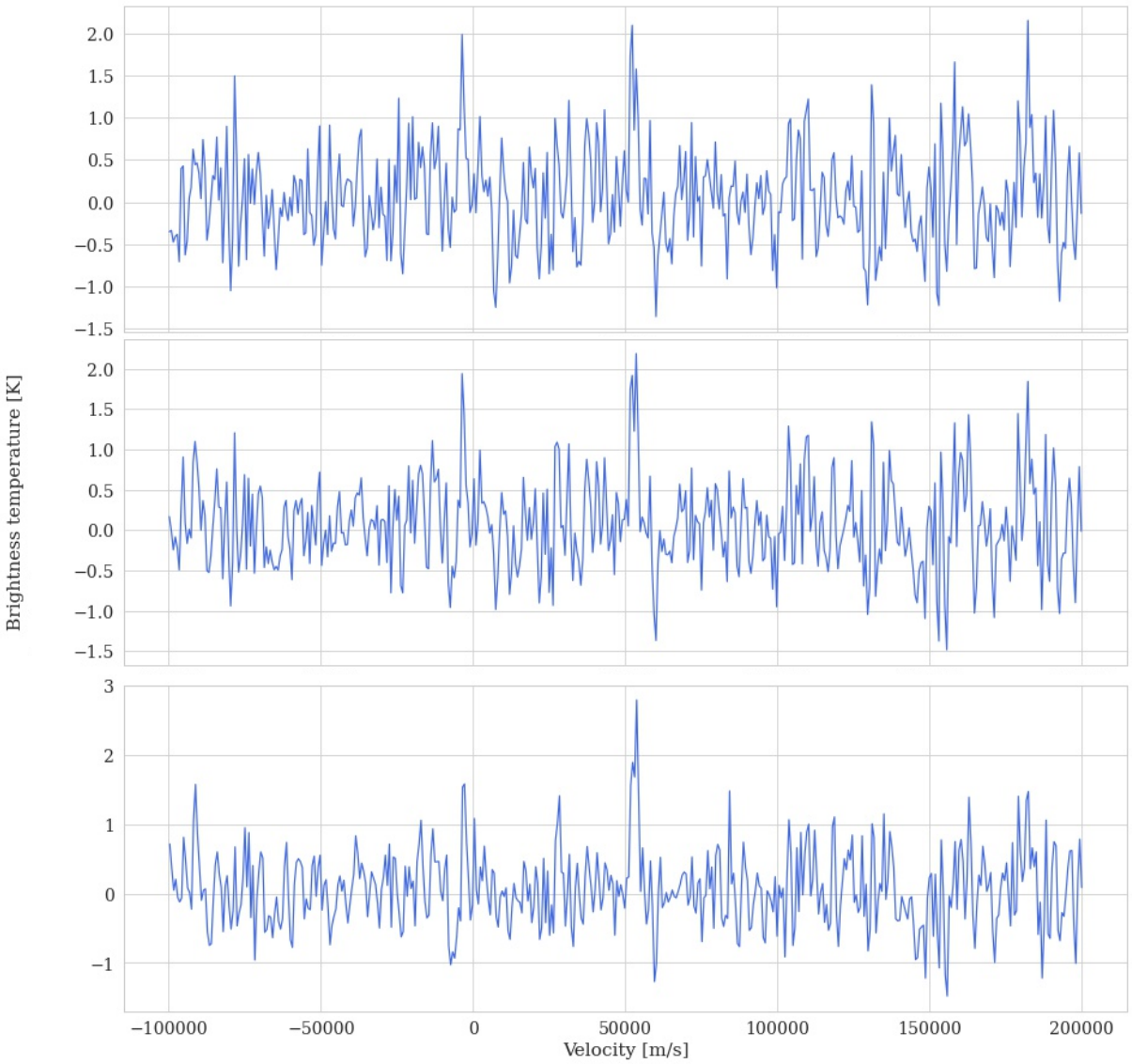

Figure A2: The extracted $C^{18}O$ spectra for region 1 (top), 2 (middle) and 3 (bottom). The spectral peaks did not meet the certainty requirement according to Section 3.2.1

DEPARTMENT OF SPACE, EARTH AND ENVIRONMENT
CHALMERS UNIVERSITY OF TECHNOLOGY
Gothenburg, Sweden 2021
www.chalmers.se

CHALMERS
UNIVERSITY OF TECHNOLOGY